

# Rigid and non-rigid registration of polarized light imaging data for 3D reconstruction of the temporal lobe of the human brain at micrometer resolution

Sharib Ali<sup>a,b,\*</sup>, Stefan Wörz<sup>a,b</sup>, Katrin Amunts<sup>c,d</sup>, Roland Eils<sup>a,b</sup>,  
Markus Axer<sup>c</sup>, Karl Rohr<sup>a,b</sup>

<sup>a</sup>*Dept. of Bioinformatics and Functional Genomics, Biomedical Computer Vision Group, BIOQUANT, IPMB, University of Heidelberg, Germany*

<sup>b</sup>*German Cancer Research Center (DKFZ), Germany*

<sup>c</sup>*Institute of Neuroscience and Medicine 1, Research Centre Jülich, Germany*

<sup>d</sup>*Cécile and Oskar Vogt Institute of Brain Research, Heinrich Heine University Düsseldorf, University Hospital Düsseldorf, Germany*

---

## Abstract

To understand the spatial organization as well as long- and short-range connections of the human brain at microscopic resolution, 3D reconstruction of histological sections is important. We approach this challenge by reconstructing series of unstained histological sections of multi-scale (1.3  $\mu\text{m}$  and 64  $\mu\text{m}$ ) and multi-modal 3D polarized light imaging (3D-PLI) data. Since spatial coherence is lost during the sectioning procedure, image registration is the major step in 3D reconstruction. We propose a non-rigid registration method which comprises of a novel multi-modal similarity metric and an improved regularization scheme to cope with deformations inevitably introduced during the sectioning procedure, as well as a rigid registration approach using a robust similarity metric for improved initial alignment. We also introduce a multi-scale feature-based localization and registration approach for mapping of 1.3  $\mu\text{m}$  sections to 64  $\mu\text{m}$  sections as well as a scale-adaptive method that can handle challenging sections with large semi-global deformations due to tissue splits. We have applied our registration method to 126 consecutive sections of the temporal lobe of the human brain with 64  $\mu\text{m}$  and 1.3  $\mu\text{m}$  resolution. Each step of the registration

---

\*Corresponding author

*Email address:* sharib.ali@eng.ox.ac.uk (Sharib Ali)

method was quantitatively evaluated using 10 different sections and manually determined ground truth, and a quantitative comparison with previous methods was performed. Visual assessment of the reconstructed volumes and comparison with reference volumes confirmed the high quality of the registration result.

*Keywords:* Image registration, 3D reconstruction, canonical correlation transform, polarized light imaging, human brain, hippocampus

---

## 1. Introduction

Decoding the connectome of the normal and pathologic human brain is one of the major goals of neuroscientists around the world. If seeking to understand the (dys-)function of the human brain, it is indispensable to study its underlying  
5 structure, i.e. the organization of neurons and their intricate connections. The mapping of the nerve fiber architecture of the human brain is a multiscale challenge as the size of the structures range from a few micrometers for the diameter of axons to several centimeters for long range inter-hemispheric connections.

3D polarized light imaging (3D-PLI) is a neuroimaging technique that offers the possibility to investigate fibers and their pathways covering the range  
10 between micro- and mesoscale, depending on the employed optical setup [1, 2]. This technique relies on transmission measurements of polarized light through thin, unstained histological brain sections in a polarimetric setup. Polarized light is an ideal probe to reveal birefringent structures in a sample. In case of  
15 brain tissue, essentially the myelinated neuronal projections referred to as nerve fibers induce birefringent properties and can therefore be discriminated from non-birefringent tissue components by polarimetry. Reckfort et al. [3] introduced a concept of combining different spatial scales by 3D-PLI measurements and pointed out the benefit of using complementary polarimeters with different  
20 optical resolutions and sensitivities. This study was based on individual 2D brain sections and not on 3D volume reconstructions. To close the spatial gap between highly resolved microscopical techniques (e.g., two-photon microscopy [4]) and the macroscopic range covered by diffusion Magnetic Resonance Imag-

ing (dMRI, [5]), high-accuracy 3D volume reconstruction from serial 3D-PLI  
25 section images is indispensable.

Previous work on the 3D reconstruction of histological brain data based  
on optical imaging (e.g., [6, 7, 8, 9, 10, 11, 12, 13, 14]) typically follows a  
common approach, where individual sections are aligned with a 3D reference  
MRI [11, 14], blockface data [7, 13], or both types of data [8, 9, 10, 6]). Dif-  
30 ferent types of registration approaches such as diffeomorphic registration based  
on demons [15] (e.g., [11, 14]), free-form deformations using B-splines [16] (e.g.,  
[8, 13]), and local rigid/affine grid schemes (e.g., [10]) have been employed.  
Mutual information [6, 8, 11] and cross-correlation [14] were used as multi-  
modal similarity measures. In addition, surface-based elastic registration using  
35 a wavelet-based multi-resolution expansion [17], block-matching [18], and poly-  
rigid and polyaffine transformation models [19] have been used for registration of  
histological sections. Most of these methods were either applied to non-human  
brain data such as rat brain (e.g., [8, 18, 17, 14]) or drosophilla brain [12], which  
are smaller and less complex than the human brain, or use only rigid or affine  
40 registration (e.g. [18, 19]), which is generally not sufficient to cope with deforma-  
tions in histological sections as mentioned in [8]. All methods mentioned above  
did not consider 3D-PLI data, which relies on unstained sections, has special  
characteristics, and is very different from traditional histological data or MRI  
data.

45 Regarding the registration of 3D-PLI data, only few work can be found [7,  
13]. In [7], a fluid model in conjunction with mutual information was used for  
registration, and a different human brain was considered compared to our work.  
In [13], 3D-PLI data of a rat brain was used. The applied non-rigid registration  
method is based on B-splines and uses the sum of square intensity differences as  
50 similarity measure. Compared to [7, 13] we use a more realistic elastic deforma-  
tion model of tissues for non-rigid registration to cope with deformations due  
to the histological sectioning procedure. We also use a different similarity mea-  
sure. In addition, our study is based on high-resolution ( $64 \mu m$ ) and ultra-high  
resolution ( $1.3 \mu m$ ) 3D-PLI data, whereas in [7] a coarser isotropic resolution of

55  $100\ \mu m$  was used and a smaller number of brain sections has been processed.

In the present study, we performed a 3D reconstruction of a coronal slab through a human temporal lobe, which includes parts of the hippocampus. The hippocampus is of specific interest in brain research, since it plays an important role for the declarative memory (e.g., [11]). Individual fiber tracts and  
60 pathways in individual sections have been analyzed in detail in a recent study by Zeineh et al. [20], while the majority of studies in the past were limited to ex vivo MRI [21, 22, 5]. In [6, 11], histological sections stained for cell bodies were registered to postmortem MRI scans, and affine as well as diffeomorphic registration utilizing normalized mutual information were applied. In [6], the  
65 3D reconstructed histological sections were used to create probabilistic cytoarchitectonic maps of the hippocampus region and its subregions. Postmortem T1-weighted MRI data with an isotropic resolution of  $1mm^3$  and acquired at 1.5 T was registered to the blockface images using an affine transformation. In [11], an isotropic resolution of  $200\ \mu m$  was used to reconstruct the human  
70 hippocampal regions from stained histology images and ex vivo MRI data. In contrast, in our work we use 3D-PLI data of the hippocampus with a much higher resolution and consider unstained histological sections.

In the present study, we introduce an intensity-based non-rigid registration method based on a physical deformation model that can handle both small and  
75 large deformations present in multi-scale and multi-modal 3D-PLI images. We also propose a complete pipeline for 3D reconstruction of spatially misaligned 3D-PLI data at both meso- and micro-scales. This work extends our previous conference paper [23], where non-rigid registration was used to cope with brain tissue deformations in high-resolution 3D-PLI images. However, there ultra-  
80 high resolution images were not considered and only 60 sections were utilized for 3D reconstruction. In addition, a different registration method was used (e.g., different similarity measure and regularization). To our knowledge, this is the first time that a 3D reconstruction is performed using a large stack of unstained histological sections of the human temporal lobe and the hippocampus  
85 region based on 3D-PLI data at both high-resolution and ultra-high resolution.

Our main contributions include: 1) introduction of a similarity metric for spline-based non-rigid registration using the canonical correlation transform, 2) rigid registration of multi-modal data based on the correlation transform, 3) regularization of the deformation vector field using a separable filter, 4) structure preserving diffusion to reduce outliers of deformation field updates in the multi-resolution energy minimization scheme, 5) scale-adaptive non-rigid registration method to tackle large semi-global deformations due to tissue splits, 6) feature-based localization and registration using a feature strength measure, and 7) a complete pipeline for 3D reconstruction of both high-resolution ( $64\ \mu m$ ) and ultra-high resolution ( $1.3\ \mu m$ ) 3D-PLI data.

This paper is organized as follows: In Section 2 we briefly describe the tissue preparation and 3D-PLI image acquisition. Section 3 presents our proposed non-rigid registration method and introduces the multi-modal similarity metric as well as different regularization schemes. In Section 4, we describe an extension of our non-rigid registration method to cope with large deformations due to tissue splits in the 3D-PLI data. Section 5 presents a feature-based localization approach for identifying ultra-high resolution image regions within the corresponding registered high-resolution images. Section 6 describes our complete pipeline for 3D reconstruction of multi-modal and multi-scale 3D-PLI data. In Section 7, we present a quantitative evaluation of our method and a comparison with existing methods. In Section 8, we discuss the main findings of our work. Finally, in Section 9 conclusions are provided.

## 2. 3D polarized light imaging

### 2.1. Preparation of human brain tissue

The process of mapping the axonal architecture in human brain sections has been described in detail in [1, 2]. In this study, the human brain of a 64-year-old male was obtained through the body donor program of the University of Rostock, Germany, in accordance with the local ethics committee. The brain was removed from the skull, and fixed in 4% formalin. A slab of the temporal

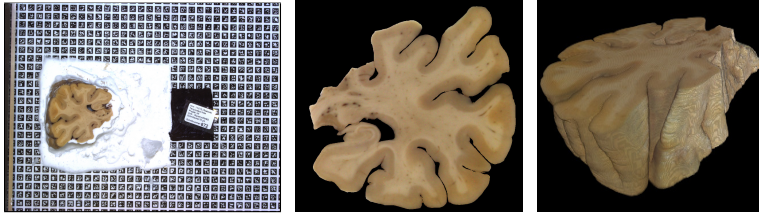


Figure 1: Temporal lobe of a human brain: Image of the temporal lobe with ARTag during sectioning (left), blockface (masked) image of a mid-section (middle), and 3D reconstructed blockface volume after rigid registration.

115 lobe of the left hemisphere was separated, cryo-protected with 20% glycerin, and frozen. The tissue was sectioned coronally at  $70 \mu m$  thickness using a large-scale cryostat microtome (Polycut CM 3500, Leica, Germany). Each histological section was mounted on a glass slide with 20% glycerin and cover-slipped. No staining was applied. Blockface images were acquired before each sectioning step  
 120 using a CCD camera mounted vertically above the frozen brain block to obtain undistorted reference images (see Fig. 1). These blockface images were serially aligned by rigid registration of the fiducial marker system ARTag mounted underneath the frozen block of tissue [24, 25].

## 2.2. Image acquisition

125 Each histological brain section was subjected to two complementary polarimetric setups [2]:

- i. a large-area polarimeter with tilting stage for acquiring images at meso-scale resolution (pixel size:  $64 \mu m \times 64 \mu m$ ) covering the entire temporal lobe (see Fig. 2 (top)), and
- 130 ii. a polarizing microscope for acquiring much more detailed image information at micro-scale resolution (pixel size:  $1.3 \mu m \times 1.3 \mu m$ ) covering a specific region of interest, the hippocampus (see Fig. 2 (bottom)).

In the following, images acquired under condition (i) will be referred to as HR (high-resolution), while images obtained according to (ii) will be referred  
 135 to as uHR (ultra-high-resolution). Both HR and uHR images are used in our

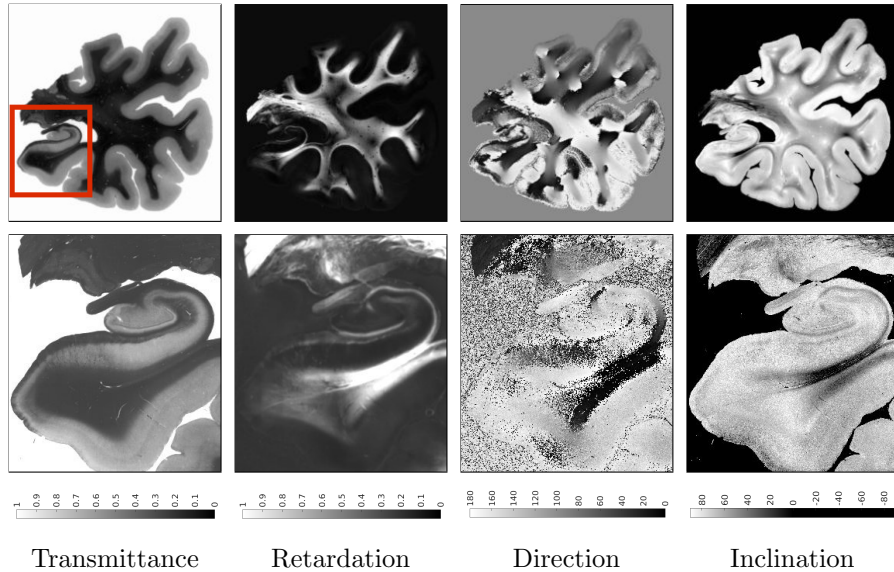


Figure 2: Different 3D-PLI modalities of the section in Fig.1 (middle).  $64\mu m$  high-resolution (HR) image (top) and  $1.3\mu m$  ultra-high resolution (uHR) images (bottom) are shown. The uHR images correspond to the marked ROI (red rectangle, top left) of the HR images.

3D reconstruction pipeline. Details on the polarized light imaging technique employed in our work can be found in the Supplementary material. We have applied our registration method to 126 consecutive sections of 3D-PLI data of the temporal lobe of the human brain. The image size for the HR images is about  $2776 \times 2080$  pixels and that for the uHR images is about  $22000 \times 15000$  pixels. In  $z$ -direction, the 3D reconstructed volume comprises  $0.88\text{ cm}$  of the temporal lobe of the human brain.

### 3. Intensity-based non-rigid registration

To cope with local deformations during the sectioning and mounting processes in the 3D-PLI data of the human brain sections, we propose an intensity-based non-rigid registration method based on a physical deformation model. 3D-PLI images of each section are registered to their corresponding blockface images.

Let  $\mathbf{u}$  be the displacement vector field (or deformation field) within the image domain  $\Omega$ ,  $\mathbf{u} = (u_1, u_2) : \Omega \rightarrow \mathbb{R}^2$ , which we aim to compute between the

150 target image  $g_1$  and the source image  $g_2$ . Then, the proposed intensity-based registration method can be formulated by an energy minimization scheme

$$E(\mathbf{u}, \mathbf{u}^I) = \phi_{data}(g_1, g_2, \mathbf{u}^I) + \underbrace{\lambda_I \psi_I(\mathbf{u}, \mathbf{u}^I) + \lambda_E \psi_{elastic}(\mathbf{u})}_{\phi_{reg}(\mathbf{u})}, \quad (1)$$

where  $\mathbf{u}^I : \Omega \rightarrow \mathbb{R}^2$  is a second deformation field which is computed using intensity information only. The first term  $\phi_{data}$  in Eq. (1) represents an *intensity similarity measure* between the deformed source and the target image. The second term  $\psi_I$  *couples* the intensity-based deformation field  $\mathbf{u}^I$  with the overall deformation field  $\mathbf{u}$  and acts as a regularizer of the two deformation fields. Finally, the third term  $\psi_{elastic}$  represents the *regularization* of the deformation field  $\mathbf{u}$  based on the elastic energy according to the Navier equation of linear elasticity [26]. The weighting factors  $\lambda_I, \lambda_E > 0$  control the trade-off between the data term  $\phi_{data}$  and the two regularization terms  $\phi_{reg}(\mathbf{u})$ . Below, we describe each component of  $E(\mathbf{u}, \mathbf{u}^I)$  as well as the minimization strategies used to compute the deformation fields.

Our non-rigid registration method comprises a novel similarity measure for the data term  $\phi_{data}$  which is based on the correlation transform and exploits similarity information of the local neighborhood to increase the robustness and accuracy. In addition, to further improve the robustness and cope with outliers in the deformation field, our method includes two regularization terms: 1)  $\psi_{elastic}$  which is based on the Navier equation of linear elasticity allowing realistic deformations of tissues, and 2)  $\psi_I$  which penalizes high variations between the computed intensity-based deformation field  $\mathbf{u}^I$  and the overall deformation field  $\mathbf{u}$ . In addition, we propose a novel type of weighting for  $\psi_I$  using a separable filter (see below). Our method is based on an analytic solution using matrix-valued Gaussian elastic body splines (GEBS, [27]). Additionally, we use a coarse-to-fine multiresolution scheme and structure preserving diffusion filtering [28] during upsampling to suppress outliers and to preserve discontinuities in the deformation fields at image boundaries.

### 3.1. Data term based on the canonical correlation transform

For the data term  $\phi_{data}$  in Eq. (1) we introduce a *canonical local correlation transform*. The correlation transform is based on  $z$ -normalized pixel intensities  $\tilde{g}(\mathbf{x})$  within a square patch  $P_{\mathbf{x}}$  centered at  $\mathbf{x}$  and defined by

$$\tilde{g}(\mathbf{x}) = \frac{g(\mathbf{x}) - \mu_g}{\sigma_g}, \quad (2)$$

where  $g(\mathbf{x})$  are the original image intensities, and  $\mu_g$  and  $\sigma_g$  are the mean intensity and the standard deviation computed within  $P_{\mathbf{x}}$ , respectively. In our previous work, we used the correlation transform of a pixel (CoT, [23]) as the data term and found that this yields better results than mutual information (MI, [29]). However, a main limitation of this approach is that it does not fully exploit the intensity characteristics within a patch since only the center pixel is taken into account. Considering the full CoT (i.e., all  $z$ -normalized pixels within a patch), the normalized cross-correlation (NCC) was formulated as a sum-of-squared differences [30], for a given pixel  $\mathbf{x}$  in a square patch  $P_{\mathbf{x}}$  of the target and the source images  $g_1$  and  $g_2$ , respectively, as

$$1 - NCC(g_1(\mathbf{x}), g_2(\mathbf{x} + \mathbf{u})) = \frac{1}{2N} \sum_{\mathbf{x}_j \in P_{\mathbf{x}}} (\tilde{g}_1(\mathbf{x}_j) - \tilde{g}_2(\mathbf{x}_j + \mathbf{u}))^2 \quad (3)$$

where  $N$  is the total number of pixels in each patch, and  $\mathbf{u}$  is the deformation vector field. Minimizing Eq. (3) corresponds to maximizing NCC. A limitation of the full CoT is that the gradient needs to be computed for all  $N$  pixels which significantly increases the computation time (e.g., for a  $7 \times 7$  patch as in our case, the gradient needs to be computed at 49 pixels). In this contribution, we propose exploiting the full information from the local neighborhood by considering the full CoT of a patch  $P_{\mathbf{x}}$  while reducing the computation time significantly. For this, we introduce the *canonical CoT* (CnCoT,  $\dot{g}(\mathbf{x})$ ), which combines the  $z$ -normalized pixels of a patch  $P_{\mathbf{x}}$  by representing them as a matrix  $\mathbf{P}$  and computing the ratio of the trace and the largest eigenvalue  $\lambda_{max}$  of  $\mathbf{P}$ . For computing  $\lambda_{max}$ , we used the Schur decomposition. Further, we use the absolute value of CoT to make the transform more independent of contrast differences.

Also, we clip the standard deviation  $\sigma_g$  using a threshold  $T_\sigma$  to avoid division by zero or small values in homogeneous regions. For computing  $\mathbf{P}$ , we use the transformation

$$\check{g}(\mathbf{x}_j) = \frac{|g(\mathbf{x}_j) - \mu_g|}{clip(\sigma_g, [T_\sigma, \infty])}, \quad \forall j \in P_{\mathbf{x}}, \quad (4)$$

where  $clip(\cdot)$  is a function which replaces values below the threshold  $T_\sigma$  (we used  $T_\sigma = 0.1 \cdot \sigma$ ). Then, our *canonical correlation transform (CnCoT)* is defined by

$$\dot{g}(\mathbf{x}) = \frac{1}{n} \frac{\text{tr } \mathbf{P}}{\lambda_{max} + \epsilon}, \quad (5)$$

where  $n$  is the number of diagonal elements of  $\mathbf{P}$ , and  $\epsilon = 0.001$  is used to prevent division by zero. Thus, the data term can be written as

$$\phi_{data}(g_1, g_2, \mathbf{u}^I) = \sum_{\mathbf{x} \in \Omega} (\dot{g}_1(\mathbf{x}) - \dot{g}_2(\mathbf{x} + \mathbf{u}^I))^2. \quad (6)$$

### 3.2. Regularization of the deformation field

In our non-rigid registration method the regularization of the deformation field is represented by  $\phi_{Reg}(\mathbf{u}) = \lambda_I \psi_I(\mathbf{u}, \mathbf{u}^I) + \lambda_E \psi_{elastic}(\mathbf{u})$  (see Eq. (1)). We use the following types of regularizations:

1. The term  $\psi_{elastic}$  represents an *elastic regularizer* based on the force-free Navier equation of linear elasticity [31]

$$\lambda_E \psi_{elastic}(\mathbf{u}) = \lambda_E \int_{\mathbf{x} \in \Omega} \frac{\mu}{4} \sum_{j,k=1}^2 (\partial_{x_j} u_k + \partial_{x_k} u_j)^2 + \frac{\lambda}{2} (\text{div } \mathbf{u})^2 d\mathbf{x} \quad (7)$$

which quantifies the strain of an object undergoing deformations.  $\psi_{elastic}$  is the regularizer corresponding to the analytic solution for the overall deformation field  $\mathbf{u}$  given in Eq. (14) below.

2. The term  $\psi_I$  represents a *weighted quadratic regularization* ( $l_2$ -norm). This term couples the intensity-based deformation field  $\mathbf{u}^I$  with the overall deformation field  $\mathbf{u}$ . In previous work [26], a Gaussian function was used for weighting. Here, we suggest using a different weighting  $f_{\sigma, \alpha}(\mathbf{x})$  based on a separable filter [32] with normalization constant  $1 - \alpha$ . An advantage

of this type of weighting is that it constrains the deviations between  $\mathbf{u}^I$  and  $\mathbf{u}$  leading to smooth deformations.

$$\lambda_I \psi_I(\mathbf{u}, \mathbf{u}^I) = \lambda_I \int d\mathbf{x} \int d\xi f_{\sigma,\alpha}(\|\mathbf{x} - \xi\|) \|\mathbf{u}^I(\xi) - \mathbf{u}(\mathbf{x})\|^2, \quad (8)$$

185 where  $f_{\sigma,\alpha}(\mathbf{x}) = \mathbf{det}(\mathbf{h}(\mathbf{x}))$ ,  $\mathbf{h}(\mathbf{x}) = \frac{e^{-\|\mathbf{x}\|^2}}{\sqrt{2\pi\sigma^2(1-\alpha)}} \begin{bmatrix} 1 - \alpha y^2/\sigma^2 & \alpha xy/\sigma^2 \\ \alpha xy/\sigma^2 & 1 - \alpha x^2/\sigma^2 \end{bmatrix}$  and  $\alpha \in [0, 0.5]$ . The separable filter  $\mathbf{h}(\mathbf{x})$  becomes a classical Gaussian filter for  $\alpha = 0$ . Experimentally we found that the normalized separable filter improves the results (see below).

3. In addition to the regularization described above, we use a coarse-to-fine multi-resolution scheme as well as structure preserving diffusion filtering [28] for the deformation field during upscaling. The computed deformation vector field  $\mathbf{u}^j$  at pyramid level  $j$  is used as initialization at the upper level  $j - 1$ . However, extrapolating  $\mathbf{u}^j$  generally amplifies outliers resulting in poor initialization for the next higher level. Therefore, we use a structure preserving filter  $\mathcal{D}_t$  during each update of the multi-resolution scheme:

$$\begin{aligned} \dot{g}_1(\mathbf{x}) &= \dot{g}_2(\mathbf{x} + \mathbf{u}^j(\mathbf{x})) \\ \mathbf{u}^{j-1}(\mathbf{x}) &= \mathcal{D}_t * \frac{\mathbf{u}^j(\mathbf{x})}{\gamma}, \end{aligned} \quad (9)$$

190 where  $\mathcal{D}_t = |\nabla \mathbf{u}| \nabla \cdot \eta(|\nabla \mathbf{u}|) \frac{\nabla \mathbf{u}}{|\nabla \mathbf{u}|}$  with conductance  $\eta$  (we used  $\eta = 0.02$ ),  $\mathcal{D}_t \geq 0$ , and  $\gamma$  is the upscaling factor.

### 3.3. Minimization strategy

Our objective is to obtain smooth and realistic deformation fields. The intensity-based deformation field  $\mathbf{u}^I$  in Eq. (1) is computed by minimizing the energy functional  $E(\mathbf{u}, \mathbf{u}^I)$  w.r.t. the first two terms, i.e. the data term  $\phi_{data}$  and the 195 weighted quadratic regularization term  $\psi_I$ . The overall deformation field  $\mathbf{u}$  is determined using the last two terms of  $E(\mathbf{u}, \mathbf{u}^I)$ , i.e. the weighted quadratic regularization term  $\psi_I$  and the elastic regularizer  $\psi_{elastic}$ . In this case, we exploit an analytic solution given by Gaussian elastic body splines (GEBS, [27]). Below,

we detail the GEBS approach and the used optimization strategy to minimize  $E(\mathbf{u}, \mathbf{u}^I)$ .

### 3.3.1. Gaussian elastic body splines

GEBS are based on the Navier equation of linear elasticity [31]

$$\mu\Delta\mathbf{u} + (\lambda + \mu)\nabla(\operatorname{div}\mathbf{u}) + \mathbf{f} = \mathbf{0} \quad (10)$$

with the deformation field  $\mathbf{u}$ , the body forces  $\mathbf{f}$ , and the Lamé constants  $\mu, \lambda$ . Assuming Gaussian forces  $\mathbf{f}_\sigma = \mathbf{c}f_\sigma = \mathbf{c}\frac{1}{(\sqrt{2\pi}\sigma)^3}\exp(\frac{-r^2}{2\sigma^2})$  with standard deviation  $\sigma$ ,  $r = \sqrt{x^2 + y^2 + z^2}$ , and  $\mathbf{c} = \{c_1, c_2, c_3\}$  representing coefficients that define the strength and direction of the Gaussian forces (we used  $c_k = 1$ ), then an analytic solution of Eq. (10) (up to a scaling factor) can be derived as matrix-valued basis function of Gaussian elastic body splines (GEBS) [27]

$$\mathbf{G}_\sigma(\mathbf{x}) = \left[ \left(3 - 4\nu + \frac{1}{2\hat{r}^2}\right)\frac{\operatorname{erf}(\sigma)}{r} - \frac{1}{\hat{r}\sqrt{\pi}}\frac{e^{-\hat{r}^2}}{r} \right] \mathbf{I} + \left[ \frac{\operatorname{erf}(\sigma)}{\hat{r}^2 2r^3}(2\hat{r}^2 - 3) + \frac{3}{\hat{r}\sqrt{\pi}r^3}e^{-\hat{r}^2} \right] \mathbf{x}\mathbf{x}^T \quad (11)$$

where  $\nu = \frac{\lambda}{2(\lambda + \mu)}$ ,  $\nu > 0$  is the Poisson ratio,  $\hat{r} = \frac{r}{\sqrt{2}\sigma}$ ,  $\mathbf{I}$  is a  $3 \times 3$  identity matrix, and  $\operatorname{erf}(x) := \frac{2}{\sqrt{\pi}} \int_0^x e^{-t^2} dt$  is the error function.

### 3.3.2. Energy minimization

The minimization of the energy functional  $E(\mathbf{u}, \mathbf{u}^I)$  in Eq. (1) is performed in two parts. First,  $E$  is minimized w.r.t.  $\mathbf{u}^I$ , that is, the data term  $\phi_{data}$  in Eq. (6) and the quadratic regularization term  $\psi_I$  in Eq. (8) are only used. The minimum is achieved when  $\frac{\partial E}{\partial \mathbf{u}^I} = \mathbf{0}$ , i.e.

$$\frac{\partial E}{\partial \mathbf{u}^I} = -2 \left\{ \sum_{\mathbf{x} \in \Omega} [\dot{g}_1(\mathbf{x}) - \dot{g}_2(\mathbf{x} + \mathbf{u}^I(\mathbf{x}))] \nabla^I \dot{g}_2(\mathbf{x} + \mathbf{u}^I(\mathbf{x})) + \lambda_I [\mathbf{u}^I(\mathbf{x}) - \mathbf{u}(\mathbf{x})] \right\} = \mathbf{0}. \quad (12)$$

In Eq. (12), the separable filter  $f_{\sigma, \alpha}$  from Eq. (8) is not considered to simplify the equation, i.e. we assume  $\sigma \rightarrow 0, \alpha = 0$ , but  $f_{\sigma, \alpha}$  is considered in the second part of the optimization (see below). Eq. (12) can be solved efficiently using

Levenberg-Marquardt optimization [33] (see [34] for implementation details). The gradients of the source image  $\nabla \hat{g}_2(\mathbf{x} + \mathbf{u}^I(\mathbf{x}))$  are computed using Gaussian derivative filters. Second,  $E(\mathbf{u}, \mathbf{u}^I)$  is minimized w.r.t.  $\mathbf{u}$  yielding a smooth and physically-based final deformation field  $\mathbf{u}$ . The minimum is achieved for  $\frac{\partial E}{\partial \mathbf{u}} = \mathbf{0}$  which yields (see Appendix A.1–A.3 for more details)

$$\frac{\partial E}{\partial \mathbf{u}} = \mu \Delta \mathbf{u} + (\lambda + \mu) \nabla (\operatorname{div} \mathbf{u}) + \epsilon_I \int f_{\sigma, \alpha}(\mathbf{x} - \xi) (\mathbf{u}^I(\xi) - \mathbf{u}(\mathbf{x})) d\xi = \mathbf{0}, \quad (13)$$

where  $\epsilon_I = 2 \frac{\lambda_I}{\lambda_E}$ . Eq. (13) can be solved analytically by using the Fourier transform. An explicit solution has been derived using matrix-vector convolution for the final deformation field  $\mathbf{u}$  in [26] as

$$\mathbf{u}(\mathbf{x}) = \mathbf{x} + [\phi_I * (\mathbf{u}^I(\mathbf{x}) - \mathbf{x})], \quad (14)$$

where  $\phi_I = \mathbf{G}_\sigma(\mathbf{x}) * \Omega_I(\mathbf{x})$  with  $\Omega_I(\mathbf{x})$  defined in the Fourier domain as

$$\hat{\Omega}_I(\boldsymbol{\omega}) = \epsilon_I \cdot \hat{f}_{\sigma, \alpha}(\boldsymbol{\omega}) \hat{\boldsymbol{\theta}}(\boldsymbol{\omega})^{-1}, \quad (15)$$

where “ $\hat{\cdot}$ ” represents the Fourier transform and “ $\hat{\boldsymbol{\theta}}(\boldsymbol{\omega})^{-1}$ ” is the inverse matrix of the matrix-valued function  $\hat{\boldsymbol{\theta}}$ . In the spatial domain,  $\hat{\boldsymbol{\theta}}$  is given by

$$\boldsymbol{\theta}(\mathbf{x}) = f_{\sigma, \alpha}(\mathbf{x}) \mathbf{I} + \epsilon_I \cdot \mathbf{G}_\sigma(\mathbf{x}), \quad (16)$$

205 where  $\mathbf{I}$  is a  $3 \times 3$  identity matrix, and  $\mathbf{G}_\sigma(\mathbf{x})$  is the basis function of Gaussian elastic body splines (GEBS) given in Eq. (11). The energy functional in Eq. (1) is alternately minimized w.r.t.  $\mathbf{u}^I$  and w.r.t.  $\mathbf{u}$ . This process is continued until convergence of the final deformation field  $\mathbf{u}$  is achieved. A multiresolution approach is used to cope with larger deformations and to improve the computational efficiency (see also Section 3.2 above).  
210

#### 3.4. Performance of the registration method

We have investigated the performance of the proposed spline-based non-rigid registration method using the canonical correlation transform (GEBS-CnCoT) for multi-modal synthetic data, and compared our method with previous non-rigid registration methods based on mutual information (MI, [35]), cross-correlation using  $z$ -normalized images (ANTS-CC, [36, 37]), and the correlation  
215

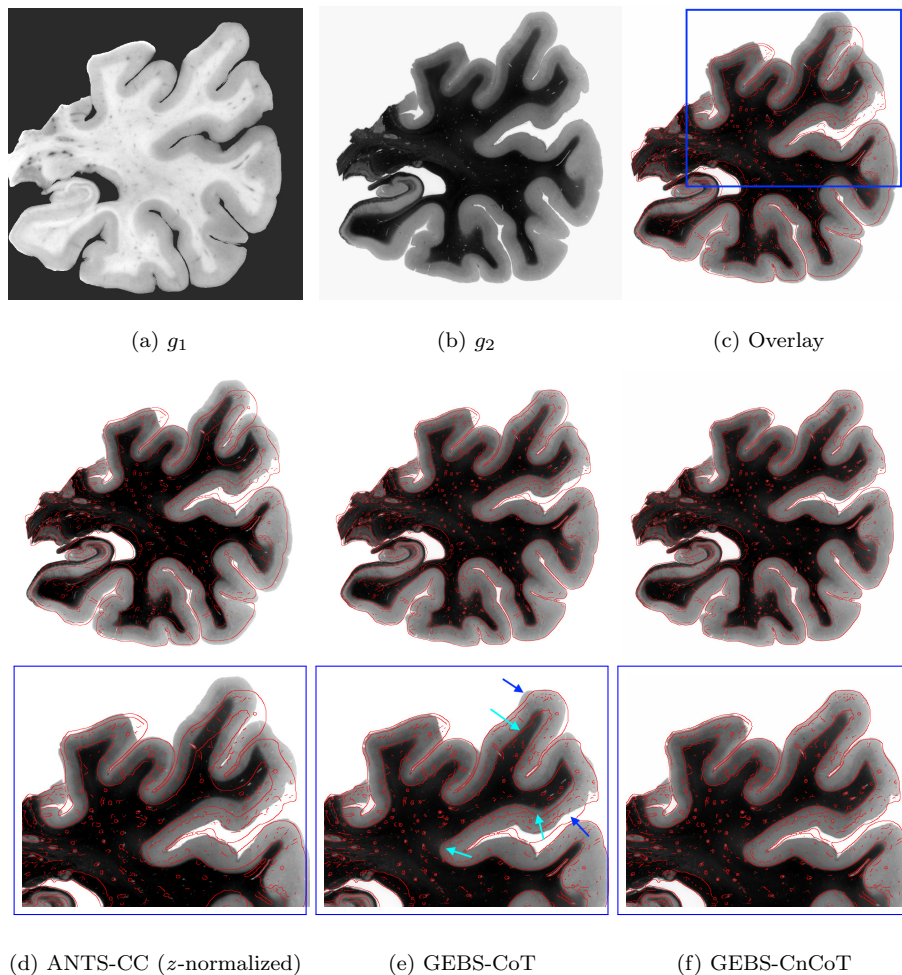


Figure 3: Non-rigid registration using different methods for real 3D-PLI data. First row: (a, b, c) Target blockface image, source transmittance image, and edge overlay. Second row: Non-rigid registration using results different methods. Third row: Corresponding results (enlarged regions) for the region indicated by the blue rectangle in (c).

transform using  $z$ -normalized images (GEBS-CoT, [23]). It turned out that the proposed GEBS-CnCoT yields the best result (see Supplementary material). To illustrate the performance of GEBS-CnCoT for real multi-modal data we use a blockface image (target image,  $g_1$ , see Fig. 3 (a)) and a 3D-PLI image (source image,  $g_2$ , see Fig. 3 (b)). In the edge overlay image in Fig. 3 (c), it

can be observed that large deformations are present at the top of the image (indicated by the blue rectangle). ANTS-CC [37] using  $z$ -normalized images can only cope with small deformations but not with large deformations (see 225 second and third row of Fig. 3 (d)). The correlation transform-based method (GEBS-CoT) [23] tackles both small and large deformations in some regions but fails in other regions (marked by cyan arrows). Also, unrealistic deformations occur as indicated by the blue arrows in Fig. 3 (e). The proposed method (GEBS-CnCoT), however, is able to tackle both small and large deformations 230 and yields realistic deformations and the best alignment (see Fig. 3 (f)).

#### 4. Scale-adaptive non-rigid registration for large semi-global deformations

During the cutting and mounting process of large-scale sections of the human brain, distortions and other artifacts such as tissue splits or foldings may be 235 introduced. In Section 3.4 above, we demonstrated that our proposed method (GEBS-CnCoT) can cope with small and large deformations in multi-modal data. However, in case of tissue splits, very large semi-global deformations occur with almost no image information in the surrounding neighborhood (see Fig. 4)(b)). In such a case, using a constant kernel size for elastic registra- 240 tion is not suitable (see Fig. 4(d)(e)). Higher values of  $\sigma_i$  also lead to stronger regularization while lower values increase the flexibility and allow coping with larger deformations. To cope with large semi-global deformations due to tissue splits, we introduce an scale-adaptive approach. We use a set of different values for the parameter  $\sigma$  of the GEBS basis function in Eq. (11) (we used 245  $\sigma_i = \{1.5, 2.5, 3.0, 4.0\}$ ) and compute deformation vector fields for each of these kernel sizes. To quantify the registration accuracy for each kernel size we use a similarity index (SI) based on the Dice coefficient and the Jaccard index using binary masks of 3D-PLI (refer to Section 5.1 below) and blockface images [24]. Then, the scale  $\sigma_i$  with the best SI value is used to perform the registration. To 250 avoid foldings of the deformation vector field, we check whether the determinant

of the Jacobian of the deformation vector field is larger or equal to zero. If this is not the case, we discard the respective deformation vector field.

From Fig. 4 (f) it can be seen that the scale-adaptive approach copes much better with large semi-global deformations compared to using a constant kernel size. The deformation grid in Fig. 4 (d) shows that with a constant setting of  $\sigma_i = 1.5$ , we have unrealistic deformations while with a constant setting of  $\sigma_i = 3$  in Fig. 4 (e) the deformations are more realistic but limited to regions

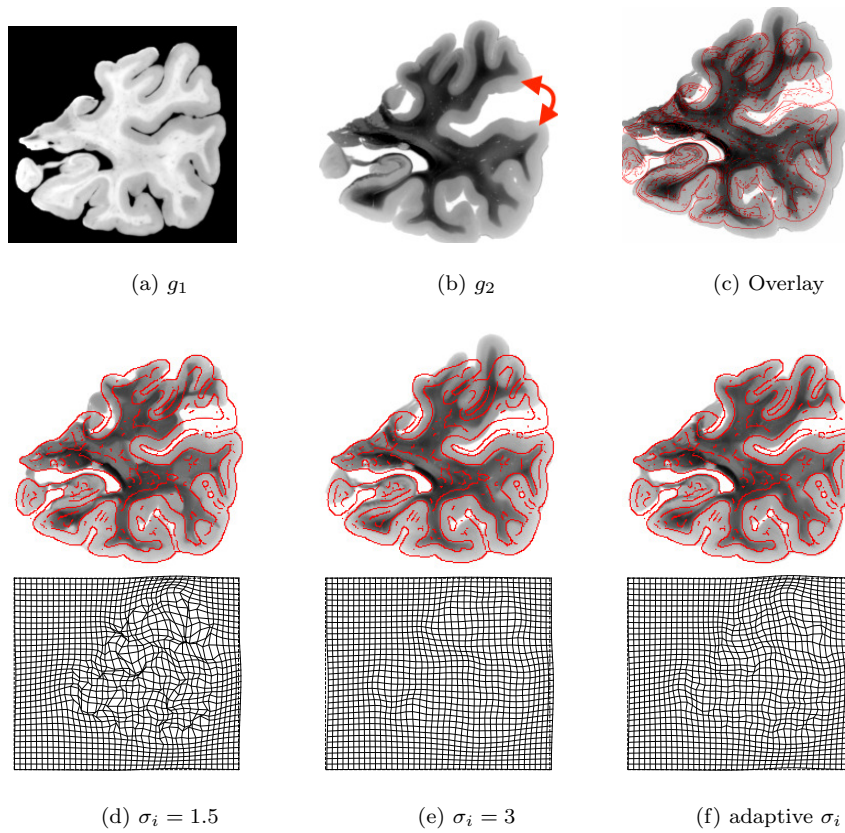


Figure 4: Non-rigid registration using scale-adaptive kernels to handle severe tissue splits. First row: (a) Target blockface image, (b) 3D-PLI image with tissue split represented by a red arrow, and (c) overlay of (a) on (b). Second row: (d, e, f) Registration results of GEBS-CnCoT for  $\sigma_i = 1.5$ ,  $\sigma_i = 3$ , and with scale-adaptive method, respectively. Results are shown for pyramid level 2. Third row: (d, e, f) Corresponding deformation grids.

with large overlaps of corresponding image structures. However, the best result is obtained by the scale-adaptive approach as can be seen in Fig. 4 (f).

## 260 5. Feature-based localization and registration

The ultra-high resolution (uHR) images of the 3D-PLI data cover only a relatively small part of the corresponding high-resolution (HR) images in the used set up (see Fig. 2). Registration of the uHR and HR images first requires accurate localization, i.e. finding the corresponding part of a uHR image as  
 265 a region-of-interest (ROI) in the HR image. Subsequently, registration is performed. Localization and registration are challenging due to i) a large difference in spatial resolution (factor of about 49), ii) a relatively small ROI (see Fig. 1), iii) regions with mostly similar image structures, iv) strong differences in intensity values, and v) arbitrary translations and orientations of the uHR images relative to the HR images. In this section, we describe a multi-scale feature-based localization and registration approach, which is based on our previous conference paper [38]. However, unlike [38], we here use a larger set of consecutive uHR and HR images, and register each uHR image to the corresponding HR image which was rigidly registered to the blockface image.

### 275 5.1. Robust feature detection

Our localization approach is based on robust feature detection using differential operators. We use a Hessian-based feature strength measure in a Gaussian scale space  $L(\mathbf{x}; \sigma_i)$  that is suitable both for uHR and HR images of 3D PLI data [38]:

$$\mathcal{S}_i = \sigma_i^2 \cdot \left( \det \mathcal{H} + \underbrace{w \cdot (\det \mathcal{H} - \lambda_1^2)}_{\mathcal{E}} \right), \quad (17)$$

where  $\det \mathcal{H} = \lambda_1 \cdot \lambda_2$  is the determinant of the Hessian matrix  $\mathcal{H}$  with eigenvalues  $\lambda_1$  and  $\lambda_2$ ,  $w = 1 - \frac{\lambda_2}{2 \cdot \lambda_1}$  is a weight depending on the shape of image structures, and  $\sigma_i^2$  is used for scale normalization. The term  $\mathcal{E}$  in (17) is close to zero for blob-like structures ( $\lambda_1 \approx \lambda_2$ ) and hence only  $\det \mathcal{H}$  is exploited. However, for elliptical  
 280 structures,  $\mathcal{E}$  contributes to  $\mathcal{S}_i$  with its strong discriminative behavior between

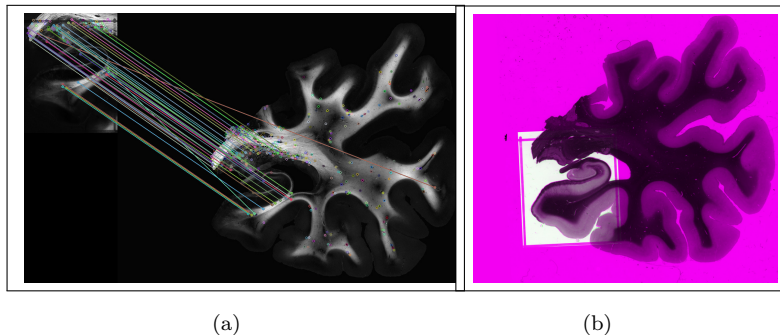


Figure 5: Localization and registration of ultra-high resolution images. (a) Establishing correspondence between uHR and (rigidly registered to the reference blockface images) HR retardation maps, and (b) color overlay (HR in magenta, uHR in green) after similarity transformation of the uHR image using matched correspondences in (a).

circular shapes ( $\lambda_1 = \lambda_2$ ) and elliptical shapes ( $\lambda_1 > \lambda_2$ ) in contrast to  $\det\mathcal{H}$ . Since only salient features are preserved due to larger discrepancy of  $\mathcal{S}_i$  between image structures, matching ambiguities are minimized. This is important for 3D-PLI images since they include many similar structures at multiple locations.

285 We used four different scales for feature computation in Gaussian scale space for  $\mathcal{S}_i$  ( $\sigma_i \in \{2.5, 5, 7.5, 10\}$ ). The maximum response within a  $3 \times 3$  window is used for extracting the final feature points  $\mathbf{x}_k$ .

### 5.2. Feature descriptor, matching, and registration

We compute SURF-like feature descriptors [39] using Gaussian derivative filters

290 (unlike [39] where Haar wavelets are used) to better preserve rotation invariance which is important for the registration of 3D-PLI data. For each feature point  $\mathbf{x}_k$ , a dominant orientation within a circular radius of  $6\sigma_i$  centered at  $\mathbf{x}_k$  is estimated. For each of the image points in this circular region, the gradient  $\nabla L^k = (L_x^k, L_y^k)^T$  is computed at scale  $\sigma_i$  by convolution with first-order Gaussian derivative filters. The dominant orientation  $\theta_k$  of the feature point  $\mathbf{x}_k$  is

295 obtained as the maximum of the sum of the weighted gradients within a sliding circle segment of  $\frac{\pi}{3}$ . For each scale, the feature descriptor comprises in total 64 values that are computed on a  $4 \times 4$  grid. For each grid position, the values

$\sum L_x$ ,  $\sum L_y$ ,  $\sum |L_x|$ , and  $\sum |L_y|$  are computed by summing up the components  
 300 in a  $2 \times 2$  neighborhood. The whole descriptor vector is re-oriented along the  
 dominant direction  $\theta_k$  as in [39].

The proposed salient feature detector (Sect. 5.1) and the feature descriptors  
 described in this section are applied both to the transmittance and retardation  
 modalities of the uHR and HR 3D-PLI data. The computed feature descriptors  
 305 are matched using a FLANN-based matcher [40] with 2-nearest neighborhood  
 connectivity. The number of the correctly matched feature points whose connect-  
 ing lines have same direction confirms the localization of the uHR region  
 within the HR counterpart (see Fig. 5). Using the matched points we compute  
 a similarity transformation (rigid transformation plus scaling) which maps  
 310 the uHR image to the HR counterpart (see white region in Fig. 5 (b)). We per-  
 formed a quantitative evaluation using simulated transformations, which showed  
 that our approach outperformed state-of-the-art feature extraction methods (see  
 Supplementary material).

## 6. 3D reconstruction pipeline for 3D-PLI data

315 In this section, we present our complete pipeline for 3D reconstruction of high-  
 resolution ( $64\mu m$ ) and ultra-high resolution ( $1.3\mu m$ ) 3D-PLI data.

### 6.1. Pipeline for 3D reconstruction of high-resolution 3D-PLI data

An overview of the pipeline for the 3D reconstruction of high-resolution ( $64\mu m$ )  
 3D-PLI images is represented in Fig. 6. Registration of these images comprises  
 320 pre-processing, rigid registration, non-rigid registration, and registration quality  
 control. Below, we describe these steps in more detail.

*Pre-processing.* For registration of 3D-PLI data with blockface (BF) images,  
 localization of the brain within the 3D-PLI data is required (see Fig. 7 (a,  
 b)). To this end, we segment the brain using a two-step refinement approach  
 325 described in [23]. Then we compute the center-of-mass (COM) of the segmented

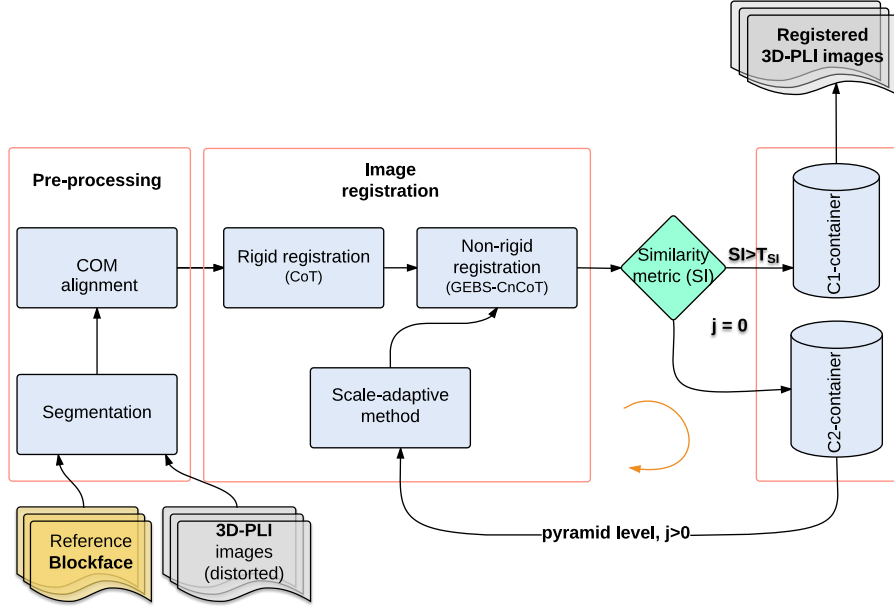


Figure 6: Pipeline for registration of high-resolution 3D-PLI images to corresponding blockface images.

BF [24] and 3D-PLI images, and compute an initial alignment by matching the COMs (see Fig. 7 (c), blockface in green and 3D-PLI image in magenta).

*Rigid registration.* We use a parametric registration model for coarse registration. Let  $g_{BF}(\mathbf{x})$  and  $g_{HR}(\mathbf{x})$  be the reference blockface image and the high-resolution image, respectively, and  $\mathcal{T}(\mathbf{x} | \theta)$  be the transformation between them with  $\theta$  denoting the set of parameters to be determined. Then, the objective is to minimize the following discrepancy function  $\psi$ :

$$\hat{\theta} = \arg \min_{\theta} \psi ( g_{BF}(\mathbf{x}), g_{HR}(\mathcal{T}(\mathbf{x} | \theta) ), \quad (18)$$

where  $\hat{\theta}$  is the optimal parameter vector. For solving Eq. (18), we use a spline-based multi-resolution rigid registration scheme [41]. In order to deal with the multi-modal data (see Figs. 1 and 2), in contrast to [41, 23], we propose using the correlation transform (CoT,  $\check{g}$ ) of the image (patch size of  $7 \times 7$  pixels). For the function  $\psi$  in Eq. (18) we use the mean squared differences between the

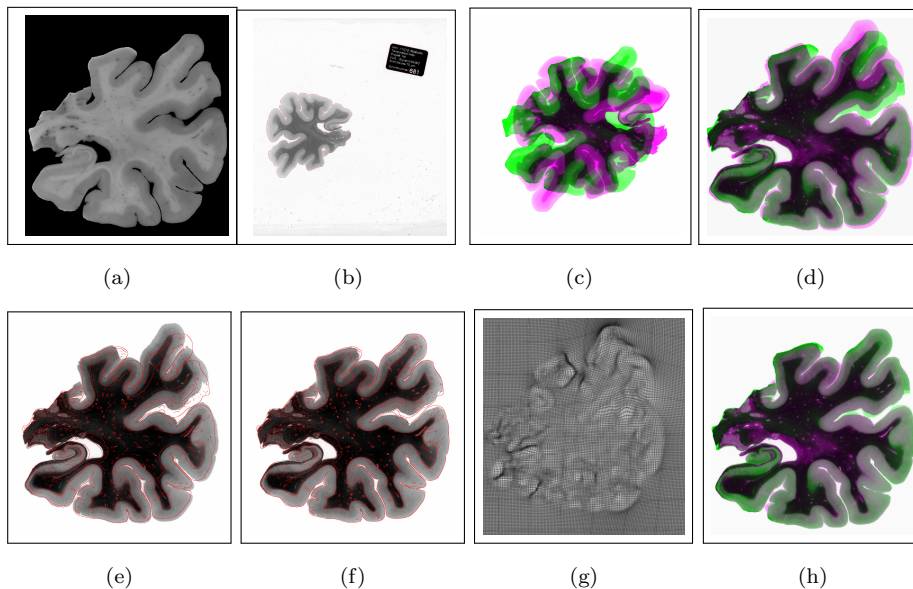


Figure 7: Registration of high-resolution 3D-PLI images. (a, b) Original blockface and transmittance map of 3D-PLI data of a human brain tissue section, (c) center-of-mass alignment with reference blockface section, (d, e) rigid registration, and (f, g, h) non-rigid registration using GEBS-CnCoT. In (c, d, h) color overlays are shown of the blockface image (green) and the 3D-PLI image (magenta), in (e, f) edge overlays of the blockface image on the 3D-PLI image are shown, and (g) provides the grid deformation.

computed CoTs for the blockface images ( $\check{g}_{BF}$ ) and the high-resolution 3D-PLI images ( $\check{g}_{HR}$ ) and apply the iterative Levenberg-Marquardt (LM) algorithm [33, 34] for minimization. 7 (d) shows a color overlay of the blockface (in green) and transmittance 3D-PLI image (in magenta) after rigid registration. It can be seen that our rigid registration approach yields a good coarse alignment, however, local misalignments are visible (e.g., see the region at the top-right). In Fig. 7 (e) a corresponding edge overlay is provided.

*Non-rigid registration.* After rigid registration, we use our intensity-based non-rigid registration method (GEBS-CnCoT) presented in Section 3 to compensate local deformations caused by the sectioning and mounting process. The employed similarity measure is based on the canonical correlation transform

(CnCoT), which is well-suited for multi-modal image registration of the 3D-PLI  
 345 images with the reference blockface (see Section 3.4 above). For our multi-  
 resolution energy minimization approach we use five pyramid levels. To ensure  
 topology preservation and realistic deformations we check whether the deter-  
 minant of the Jacobian of the deformation field is larger or equal to zero, i.e.  
 $\det(\mathbf{J}(\mathbf{u})) \geq 0$ . In case of a negative value for  $\det(\mathbf{J}(\mathbf{u}))$ , we increase the value of  
 350 the scale parameter  $\sigma$  and continue the iteration of the minimization. Our exper-  
 iments showed that using  $\sigma = 6$  always resulted in a positive value for  $\det(\mathbf{J}(\mathbf{u}))$   
 except for large tissue splits, which are coped with using the scale-adaptive  
 approach described in Section 4 above. The proposed non-rigid registration  
 method is able to tackle both small and large deformations as those in Fig. 7  
 355 (d, e). It can be seen in Fig. 7 (f, g) that the proposed non-rigid registration  
 method accurately registers the reference blockface image to the corresponding  
 high-resolution 3D-PLI image. Quantitative and qualitative evaluations of the  
 registration accuracy are described in Section 7 below.

*Registration quality control.* We use a score ( $0 \leq SI \leq 1$ ) for the registration  
 360 quality based on the similarity index SI (average of the Dice coefficient and  
 Jaccard index, each computed between binary masks of the reference blockface  
 image and the warped 3D-PLI image). If the SI value is larger than a thresh-  
 old  $T_{SI}$  (we used  $T_{SI} = 0.95$ ), we consider the registration to be successful,  
 otherwise, we use the scale-adaptive registration approach (optimization of the  
 365 parameter  $\sigma$  of the GEBS basis function, see Section 4). This approach improves  
 the registration in case of large semi-global deformations (tissue splits). In our  
 pipeline, we use a container C1 which includes all accurately registered 3D-PLI  
 images (i.e. with  $SI \geq 0.95$ ), and a container C2 which includes 3D-PLI images  
 that need to be registered using the scale-adaptive approach (see Fig. 6). For  
 370 example, for the image pair in Fig. 7 (d) we obtained a value of  $SI = 0.97$ , and  
 thus scale-adaptive registration was not needed for this case.

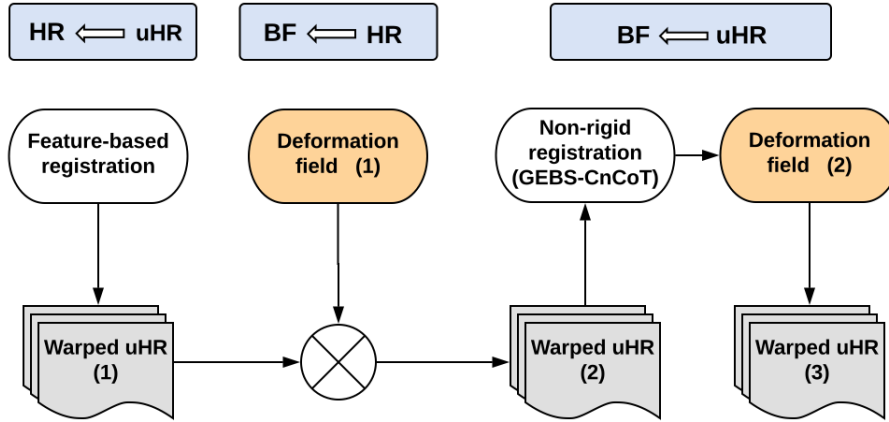


Figure 8: Pipeline for registration of ultra-high resolution 3D-PLI images to corresponding blockface images.

### 6.2. Pipeline for 3D reconstruction of ultra-high resolution 3D-PLI data

Registration of the ultra-high resolution (uHR) 3D-PLI images with the reference blockface images (BF) is achieved by the following steps: 1) feature-based  
 375 localization and similarity transformation of uHR images as described in Section 5, 2) transformation of the uHR image using the computed deformation field  
 for the HR image (see Section 6.1), and 3) non-rigid registration of the warped

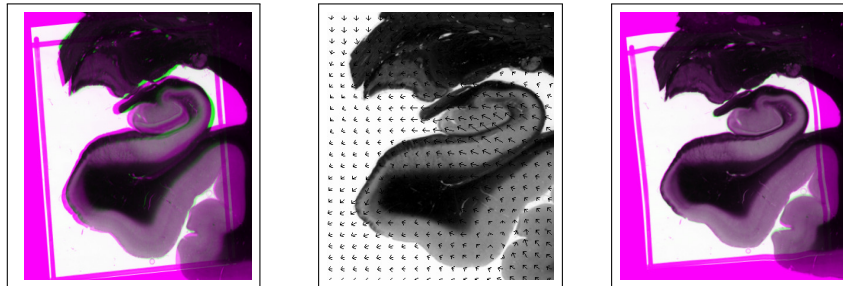


Figure 9: Registration results (color overlay) for ultra-high resolution images (hippocampus region). Left: Feature-based registration of uHR with HR (similarity transform), middle: Computed deformation vectors from non-rigid registration of uHR to blockface (scaled for visualization), and right: Registration result combining feature-based and non-rigid registration. Regions with green and magenta color inside the overlap area (white region) indicate misalignment.

uHR image to the BF image to compensate deformations caused by time de-  
lays between HR and uHR 3D-PLI image acquisitions. The overall pipeline is  
380 presented in Fig. 8.

## 7. Experiments and results

For a quantitative evaluation of the different steps of our registration method,  
we used 10 different (non-consecutive) temporal human brain sections of the HR  
(64  $\mu m$ ) and uHR (1.3  $\mu m$ ) 3D-PLI images. The sections were chosen so that  
385 the whole 3D volume is well represented. We took into account 1) difference in  
shape of brain tissue, and 2) variability of the transformation needed for regis-  
tration with the reference blockface data. As performance measure we computed  
the mean target registration error (mean TRE) for each registration step using  
an average of 106 landmarks for each section of the HR data of the temporal  
390 lobe and an average of 23 landmarks for each section of the uHR data of the  
hippocampus region. The mean TRE is computed as the mean Euclidean dis-  
tance between the ground truth positions (i.e., landmarks in BF from an expert)  
and the transformed landmark positions of the 3D-PLI data. The landmarks  
were determined by an expert (in total 1293 landmarks) by clicking with the  
395 computer mouse on the screen and using different image magnifications. It took  
about 60 hours to specify the landmarks. In addition, we used 126 consecutive  
sections from the HR and uHR 3D-PLI data to visually assess the registration  
quality in the 3D reconstructed volume.

### 7.1. Quantitative evaluation

400 Tab. 1 summarizes the results for the mean TRE for 10 different sections of the  
3D-PLI data. Each section of both the high-resolution and ultra-high resolution  
images were registered to the corresponding blockface images. For registration  
of the HR images to the blockface images the transmittance data was used, while  
for registration of the uHR images to the blockface images both transmittance  
405 and retardation images were used (see Section 5 above). As comparison with

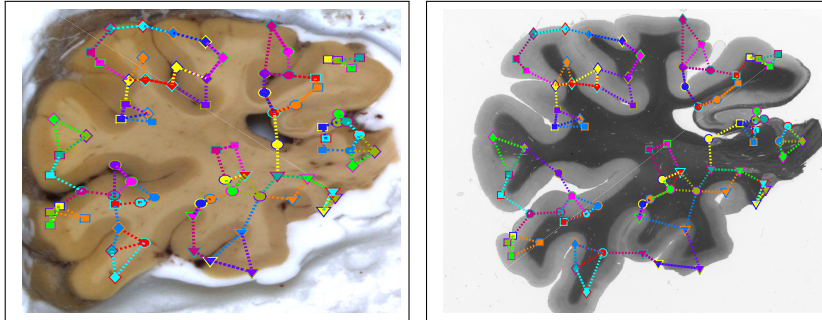


Figure 10: Ground truth landmarks. Left: Reference blockface image. Right: Corresponding high-resolution 3D-PLI image. Colored lines indicate the distance between landmarks. Images have been scaled for better visualization.

the proposed GEBS-CnCoT method we also applied three other non-rigid registration methods based on cross-correlation for  $z$ -normalized images using the non-rigid registration method of ANTS (ANTS-CC ( $z$ -normalized) [37]), mutual information using the diffeomorphic method of ANTS (ANTS-SyN-MI [36, 37])  
 410 and the correlation transform using GEBS (GEBS-CoT, [23]). We also applied ANTS with mutual information (ANTS-MI), which yielded higher target registration errors than ANTS-CC ( $z$ -normalized) and therefore was not included in Tab. 1. For all methods, the optimal parameters were determined empirically based on all 10 sections of the 3D-PLI data and kept constant for all experiments performed in this work. The parameter settings for ANTS methods are  
 415 provided in the Supplementary material.

### 7.1.1. Evaluation using the high-resolution 3D-PLI images

From Tab. 1 (left) it can be seen that the center-of-mass (COM) alignment yields very large TRE values which indicates that the high-resolution 3D-PLI  
 420 images have very large misalignments with respect to the blockface images (average TRE of 454 pixels). Using our multi-modal rigid registration method yields a significantly better result, which is further improved by non-rigid registration. It can be seen that all non-rigid registration methods generally improve the accuracy. However, the correlation transform-based GEBS methods (GEBS-

		Blockface $\Leftarrow$ High-resolution (HR)							Blockface $\Leftarrow$ Ultra-high resolution (uHR)						
Sect.	LMs	COM	CoT rigid	Non-rigid registration				LMs	COM	Simil. ttf.	Non-rigid registration				
				ANTS-CC (z-norm.)	ANTS-SyN-MI	CoT	CnCoT				ANTS-CC (z-norm.)	ANTS-SyN-MI	CoT	CnCoT	
#561	100	497.5	12.7 $\pm$ 8.7	12.0 $\pm$ 7.5	7.1 $\pm$ 4.3	<b>2.5<math>\pm</math>1.7</b>	2.6 $\pm$ 1.7	20	474.3	14.8 $\pm$ 9.8	14.8 $\pm$ 9.8	8.7 $\pm$ 6.1	4.7 $\pm$ 3.8	<b>4.2<math>\pm</math>3.6</b>	
#583	100	517.4	9.6 $\pm$ 8.7	6.5 $\pm$ 4.4	5.3 $\pm$ 4.0	<b>3.3<math>\pm</math>2.5</b>	3.5 $\pm$ 3.1	20	633.9	7.0 $\pm$ 5.7	5.2 $\pm$ 2.7	7.2 $\pm$ 4.8	5.0 $\pm$ 3.3	<b>4.4<math>\pm</math>3.7</b>	
#593	100	248.2	17.4 $\pm$ 13.8	8.8 $\pm$ 7.5	8.7 $\pm$ 8.7	6.8 $\pm$ 10.0	<b>5.2<math>\pm</math>6.7</b>	21	484.9	6.0 $\pm$ 2.4	4.6 $\pm$ 3.6	7.8 $\pm$ 6.9	4.0 $\pm$ 3.2	<b>3.9<math>\pm</math>3.0</b>	
#620	100	220.1	13.4 $\pm$ 7.5	10.8 $\pm$ 6.3	5.3 $\pm$ 4.0	3.9 $\pm$ 3.5	<b>2.8<math>\pm</math>3.1</b>	16	605.5	15.9 $\pm$ 7.3	17.5 $\pm$ 4.7	11.3 $\pm$ 9.0	8.0 $\pm$ 7.0	<b>6.1<math>\pm</math>7.2</b>	
#637	104	522.5	11.2 $\pm$ 7.9	9.5 $\pm$ 3.9	5.8 $\pm$ 3.9	4.0 $\pm$ 3.6	<b>3.5<math>\pm</math>2.8</b>	28	602.6	16.5 $\pm$ 7.7	9.9 $\pm$ 5.5	7.8 $\pm$ 4.6	6.1 $\pm$ 3.8	<b>4.3<math>\pm</math>2.9</b>	
#663	102	482.5	6.3 $\pm$ 4.5	5.3 $\pm$ 3.5	5.4 $\pm$ 3.8	<b>2.8<math>\pm</math>1.8</b>	<b>2.8<math>\pm</math>1.6</b>	25	633.9	9.0 $\pm$ 4.4	7.9 $\pm$ 4.2	8.2 $\pm$ 5.3	7.0 $\pm$ 3.5	<b>4.0<math>\pm</math>4.2</b>	
#672	96	533.9	17.6 $\pm$ 11.6	16.9 $\pm$ 10.5	5.6 $\pm$ 3.4	3.4 $\pm$ 2.7	<b>3.1<math>\pm</math>2.0</b>	14	703.4	39.3 $\pm$ 7.6	30.8 $\pm$ 7.6	11.8 $\pm$ 4.7	12.0 $\pm$ 6.5	<b>7.8<math>\pm</math>6.4</b>	
#673	122	494.2	7.9 $\pm$ 5.4	5.5 $\pm$ 3.7	5.9 $\pm$ 3.6	3.7 $\pm$ 2.8	<b>3.4<math>\pm</math>2.3</b>	32	592.6	5.7 $\pm$ 3.9	11.2 $\pm$ 5.5	8.5 $\pm$ 4.6	4.4 $\pm$ 3.4	<b>3.7<math>\pm</math>2.9</b>	
#681	123	508.5	11.7 $\pm$ 13.9	10.3 $\pm$ 6.5	6.7 $\pm$ 3.9	3.9 $\pm$ 3.5	<b>3.3<math>\pm</math>2.2</b>	24	618.6	6.6 $\pm$ 2.4	5.6 $\pm$ 3.2	5.4 $\pm$ 2.9	4.0 $\pm$ 2.7	<b>3.5<math>\pm</math>2.7</b>	
#688	118	518.6	11.6 $\pm$ 10.7	9.6 $\pm$ 5.5	7.2 $\pm$ 4.7	4.0 $\pm$ 4.2	<b>3.3<math>\pm</math>2.6</b>	28	661.1	19.9 $\pm$ 12.5	8.2 $\pm$ 3.4	16.9 $\pm$ 10.9	8.7 $\pm$ 6.0	<b>6.3<math>\pm</math>3.4</b>	
Avg.	106	454.0	11.9 $\pm$ 9.3	8.9 $\pm$ 5.9	6.3 $\pm$ 4.4	3.8 $\pm$ 3.6	<b>3.3<math>\pm</math>2.8</b>	23	661.1	14.0 $\pm$ 6.3	11.5 $\pm$ 4.6	9.4 $\pm$ 6.0	6.4 $\pm$ 4.3	<b>4.8<math>\pm</math>4.0</b>	

Table 1: Mean target registration error (in pixels) for different registration methods and for 10 different sections of the temporal lobe of the human brain registered to the reference blockface images. The high-resolution images represent the temporal lobe, and the ultra-high resolution images represent the hippocampus region of the temporal lobe.

425 CoT [23] and the proposed GEBS-CnCoT) yield a higher accuracy compared to ANTS-CC ( $z$ -normalized) [37] and ANTS-SyN-MI [36, 37]. It should be noted that ANTS was primarily developed for registration of MRI brain images [37], however, it was also utilized for registration of histological images to MRI data [14]. The mean TRE for high-resolution to blockface image registration for our proposed method (GEBS-CnCoT) is smallest for most of the sections. Compared to GEBS-CoT the improvement of the mean TRE is, for example, 1.6 pixels for section #593 and 1.1 pixels for section #620. Compared to ANTS-CC ( $z$ -normalized) and ANTS-SyN-MI, our new method yields an improvement of 5.6 pixels and 3.0 pixels, respectively, for the mean TRE averaged over all 10 sections. The mean TRE for the proposed method is 3.3 pixels while for GEBS-CoT, ANTS-SyN-MI, and ANTS-CC ( $z$ -normalized) we have 3.8, 6.3, and 8.9 pixels, respectively. In addition, the mean standard deviation is lowest for the proposed method ( $\pm 2.8$  pixels) compared to ANTS-CC ( $\pm 5.9$  pixels), ANTS-SyN-MI ( $\pm 4.4$  pixels), and GEBS-CoT ( $\pm 3.6$  pixels).

440 *7.1.2. Evaluation using the ultra-high resolution 3D-PLI images*

To quantify the registration accuracy of the ultra-high resolution images, we downsampled the uHR images to the resolution of the reference blockface images ( $64\mu m$ ). Thus, all results presented in Tab. 1 are for the  $64\mu m$  resolution, however, landmarks for uHR data were placed at the original  $1.3\mu m$  resolution.

445 From Tab. 1 (right) it can be seen that the mean TRE for center-of-mass alignment (COM) is very large (661.1 pixels). This is due to largely different rotations, translations, and scale differences between the blockface and the ultra-high resolution images. Using a similarity transformation and our feature-based registration approach (see Section 5) provides a good initial alignment with a mean TRE of  $14.0\pm 6.3$  pixels (over all 10 sections), however, most sections show very large misalignments ( $> 10$  pixels). All non-rigid registration methods improve the registration accuracy for most of the sections. However, the largest improvements are obtained by the proposed GEBS-CnCoT method, which yields the highest accuracy compared to the other non-rigid registration methods. For

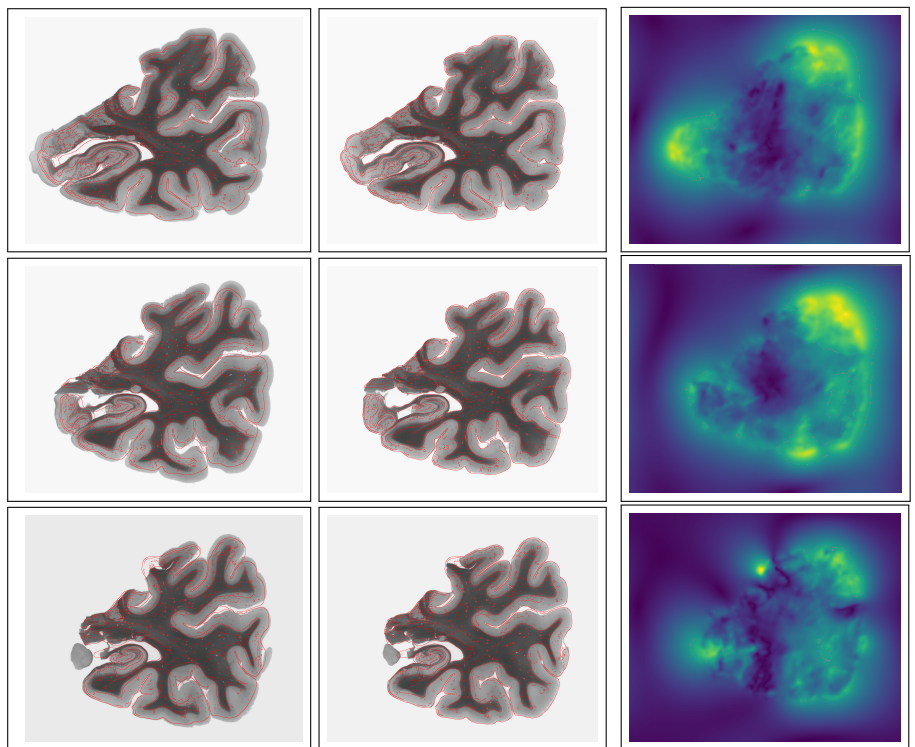


Figure 11: Non-rigid registration of three examples of the high-resolution 3D-PLI images to the corresponding reference blockface images (red contour). First column: Rigid registration, Second column: Non-rigid registration using GEBS-CnCoT. Third column: Magnitude of the deformation vector field for GEBS-CnCoT. The values for the magnitude range from zero (dark blue) to 35 pixels (yellow).

455 example, GEBS-CnCoT yields an improvement of more than 10 pixels for sections #561, #620, and #672 compared to ANTS-CC ( $z$ -normalized). Compared to GEBS-CoT there is an improvement of more than 2 pixels for sections #663, #672, and #688. The overall mean TRE for GEBS-CnCoT is  $4.8 \pm 4.0$  pixels while for ANTS-CC ( $z$ -normalized), ANTS-SyN-MI, and GEBS-CoT we have  
 460  $11.5 \pm 4.6$ ,  $9.4 \pm 6.0$  pixels and  $6.4 \pm 4.3$  pixels, respectively.

### 7.2. Visual assessment of the high-resolution 3D-PLI images

In Fig. 11 we show registration results for three examples of the high-resolution 3D-PLI images. It can be seen that after rigid registration there are relatively

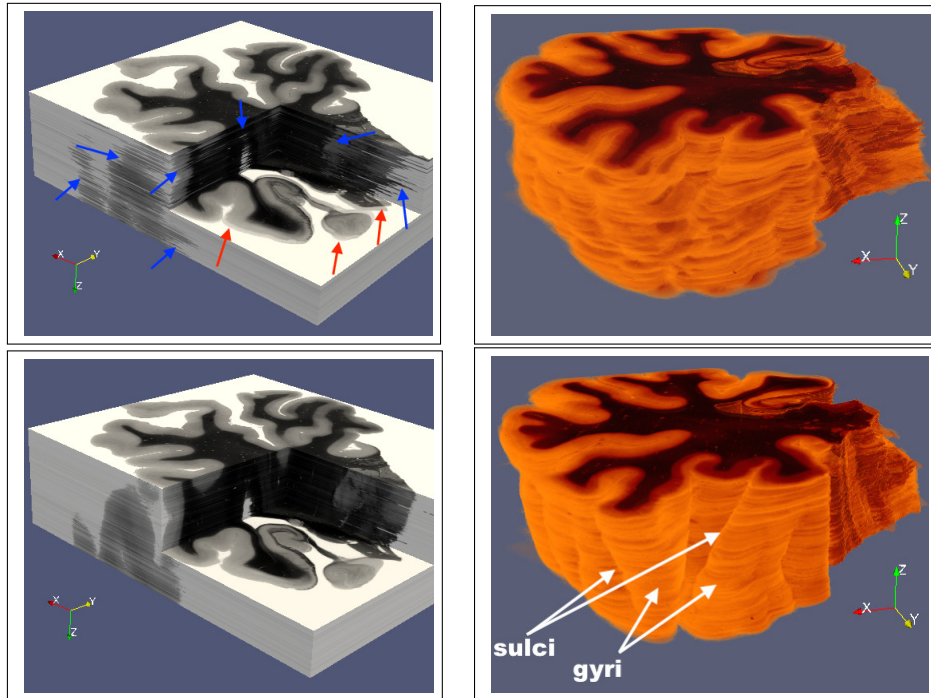


Figure 12: 3D cut-through visualization (left) and volume rendering (right) of the 3D reconstructed high-resolution images (3D-PLI, transmittance) of the temporal lobe of the human brain using rigid (top) and non-rigid registration (bottom).

large misalignments for both the internal white matter region (dark intensities) and the outer grey matter region (bright intensities) (see Fig. 11, first column).  
 465 These misalignments strongly affect the quality of the 3D reconstruction. In the 3D cut-through visualization in Fig. 12 (top), one can observe that the sections are not coherently aligned (several misaligned regions are marked by blue arrows). Due to the large misalignments ghost-like artifacts are also observed (marked by red arrows in Fig. 12 (top left)). Also the rendered 3D volume representation in Fig. 12 (top right) clearly reveals that very large misalignments are present between sections. However, after non-rigid registration using our GEBS-CnCoT method both the white matter and the grey matter regions in the 3D-PLI data are aligned well (see Fig. 11, second column). For accurate  
 470 registration, both small and large deformations are needed as indicated by the

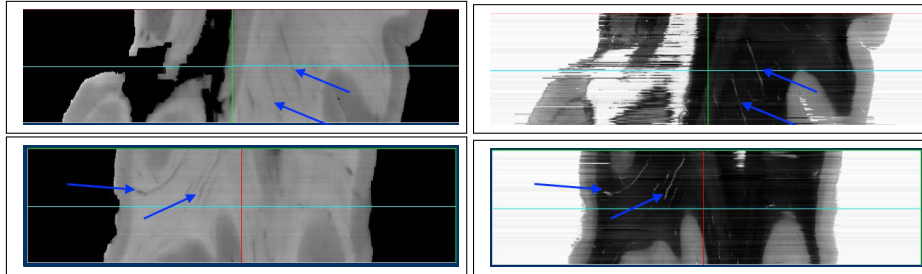


Figure 13: Reference blockface image (left) and registered 3D-PLI transmittance image (right). Shown are the  $xz$ -plane (top) and the  $yz$ -plane (bottom). Vessel structures can be observed in the white matter region at same locations for both registered modalities indicating that the images are well registered.

displayed magnitudes of the deformation field in Fig. 11 (third column). From the 3D cut-through visualization and the 3D rendering in Fig. 12 (bottom) it can be seen that the sections are coherently aligned after non-rigid registration and that the 3D reconstruction has a much better quality compared to rigid registration (Fig. 12 (top)). The observed continuity at various distinctive tissue grooves (sulci) and ridges (gyri) indicates that the sections are accurately aligned. In order to confirm the quality of the registration, we further present  $xz$ - and  $yz$ -orthogonal views of the registered 3D-PLI volume and compare them with the reference blockface volume in Fig. 13. It can be seen that the white matter and gray matter regions are coherently aligned. Additionally, in both views one can observe well reconstructed vessel structures (e.g., see the blue arrows marked in each view). For 3D-PLI, vessel structures have a higher birefringence effect compared to the fiber structures. Both the structure and location of these vessels in the registered 3D-PLI data matches to that of the blockface data. Shaded regions in Fig. 13 (right) are due to intensity variation because of differences in acquisition times and very large tissue splits in few sections, and not due to misalignment. Thus, vessel structures better indicate the quality of the alignment (blue arrows).

In Fig. 14 we show a 3D reconstruction based on 3D-PLI retardation images (which have a higher contrast in the white matter region compared to the gray

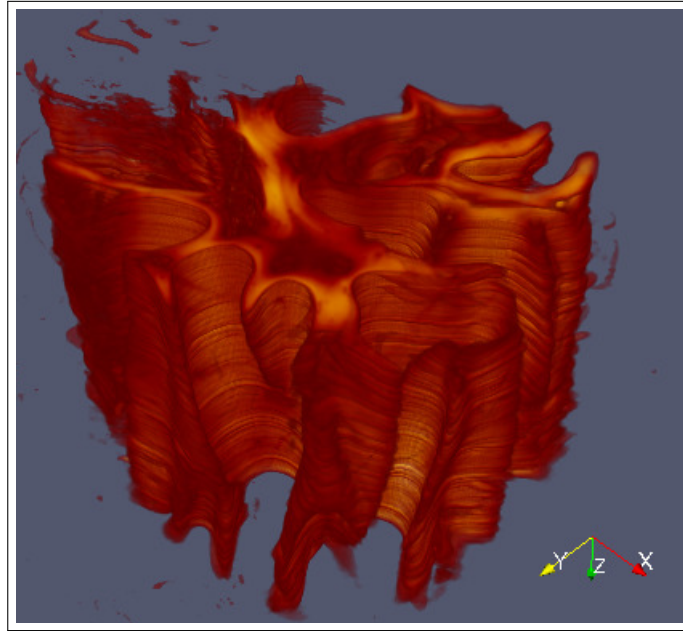


Figure 14: 3D reconstruction of the white matter region of the temporal lobe of the human brain. Retardation images of the high-resolution 3D-PLI data were used.

matter region). It can be observed that the sections are coherently registered. Few misalignments are due to missing parts (e.g., see top left region).

### 7.3. Visual assessment of the ultra-high resolution 3D-PLI images

Orthogonal views for two different subregions of the hippocampus (dentate gyrus  
 500 and cornu ammonis region) of the 3D reconstructed uHR 3D-PLI data are shown  
 in Fig. 15 (right). For comparison, the same views are provided for the reference  
 blockface volume Fig. 15 (middle). It can be seen that the reconstructed data  
 well follows the shape variations of the structures in the reference blockface data  
 at most locations (e.g., see the top right, middle, and left tissue boundaries in  
 505 both orthogonal views). The few zigzag boundaries in the reconstructed 3D-  
 PLI data are due to missing tissue parts in the sections at those locations. A  
 rendered 3D reconstructed volume of the uHR 3D-PLI data is shown in Fig. 16.  
 The 3D reconstruction also shows coherently aligned cornu ammonis (CA) and  
 dentate gyrus (DG) regions (indicated by arrows).

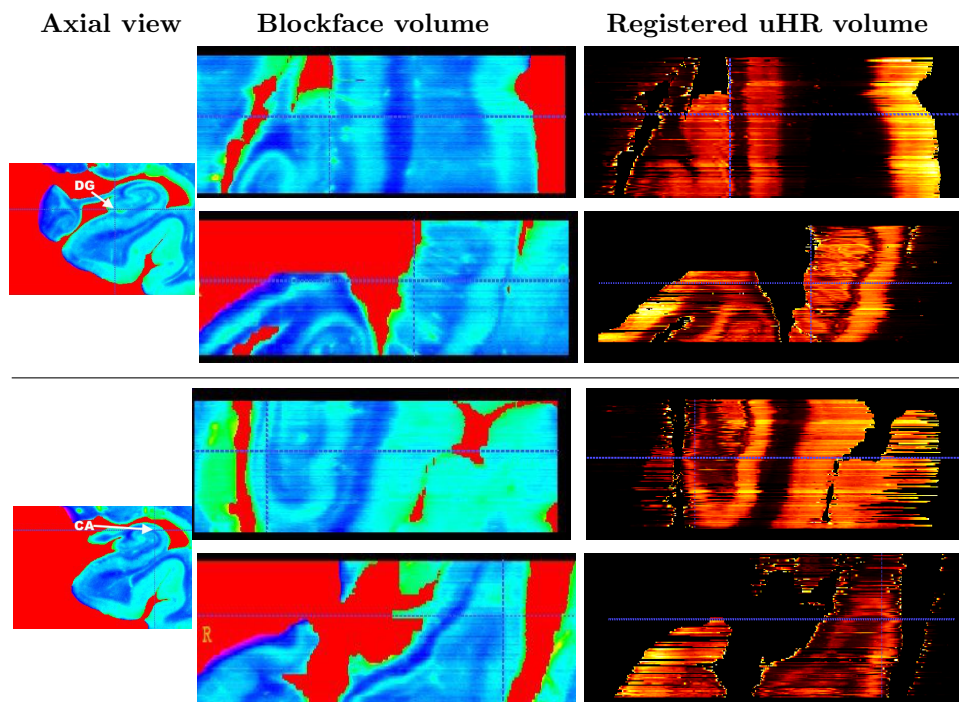


Figure 15: Coronal (top) and sagittal (bottom) views of 3D reconstructed ultra-high resolution ( $1.3 \mu\text{m}$ ) 3D-PLI volume (right) and reference blockface volume (middle) for subregions (positions indicated by cross-hairs) corresponding to the dentate gyrus (DG) and the cornu ammonis (CA) (left). Note that discontinuities at the periphery of the views are mainly due to missing brain tissue parts.

#### 510 7.4. Fiber orientation map for 3D-PLI data

Fiber orientation maps (FOMs) for registered HR ( $64 \mu\text{m} \times 64 \mu\text{m} \times 70 \mu\text{m}$ ) and uHR ( $1.3 \mu\text{m} \times 1.3 \mu\text{m} \times 70 \mu\text{m}$ ) (scaled for visualization) sections are presented in Fig. 17 (top left and top right). The FOM of an enlarged region around the hippocampus in the uHR image shown in Fig. 17 (bottom) reveals detailed  
 515 information about the fiber orientations for subregions like dentate gyrus, alveus, and cornu ammonis [20]. FOMs were computed based on the inclination and the direction images of the 3D-PLI data (for details on FOMs we refer to [1, 20]). Note that the different modalities of the 3D-PLI data at a certain resolution ( $1.3 \mu\text{m}$  or  $64\mu\text{m}$ ) are aligned. Therefore, the transformations obtained by

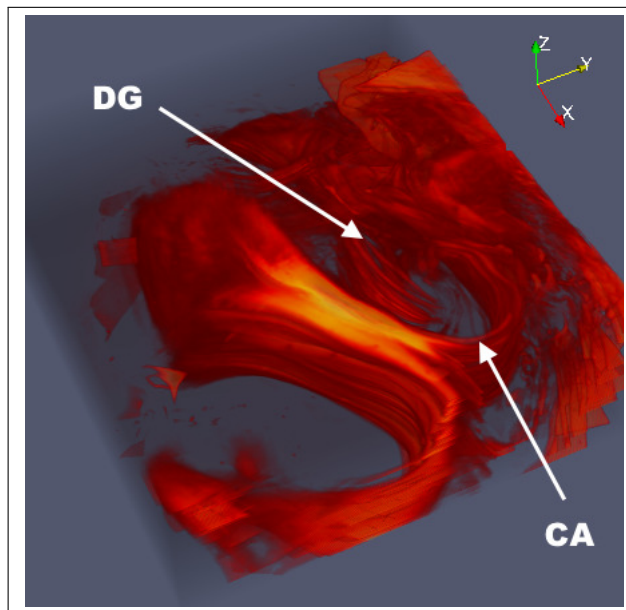


Figure 16: 3D reconstruction of ultra-high resolution 3D-PLI images ( $1.3\mu m$ , retardation). Cornus ammonis (CA) and dentate gyrus (DG) regions are indicated by arrows in the reconstructed volume.

520 registering either transmittance or retardation images can be directly applied to the inclination and direction images.

## 8. Discussion

We have presented a registration method for 3D reconstruction of multi-scale and multi-modal 3D-PLI data of the temporal lobe of the human brain. We considered 3D-PLI data acquired at  $64\mu m$  (HR data) and  $1.3\mu m$  (uHR data) resolution. While the HR data covers the whole temporal lobe region, the uHR data represents the hippocampus region. Since spatial coherence is lost during the sectioning and mounting process, registration is inevitable. To establish coherent 3D volumes, the HR and uHR 3D-PLI data are registered to the corresponding reference blockface data. Registration needs to cope with both global and local misalignments and hence both rigid (or affine) and non-rigid registration methods are required. Since brain tissue deformations occur during the

530

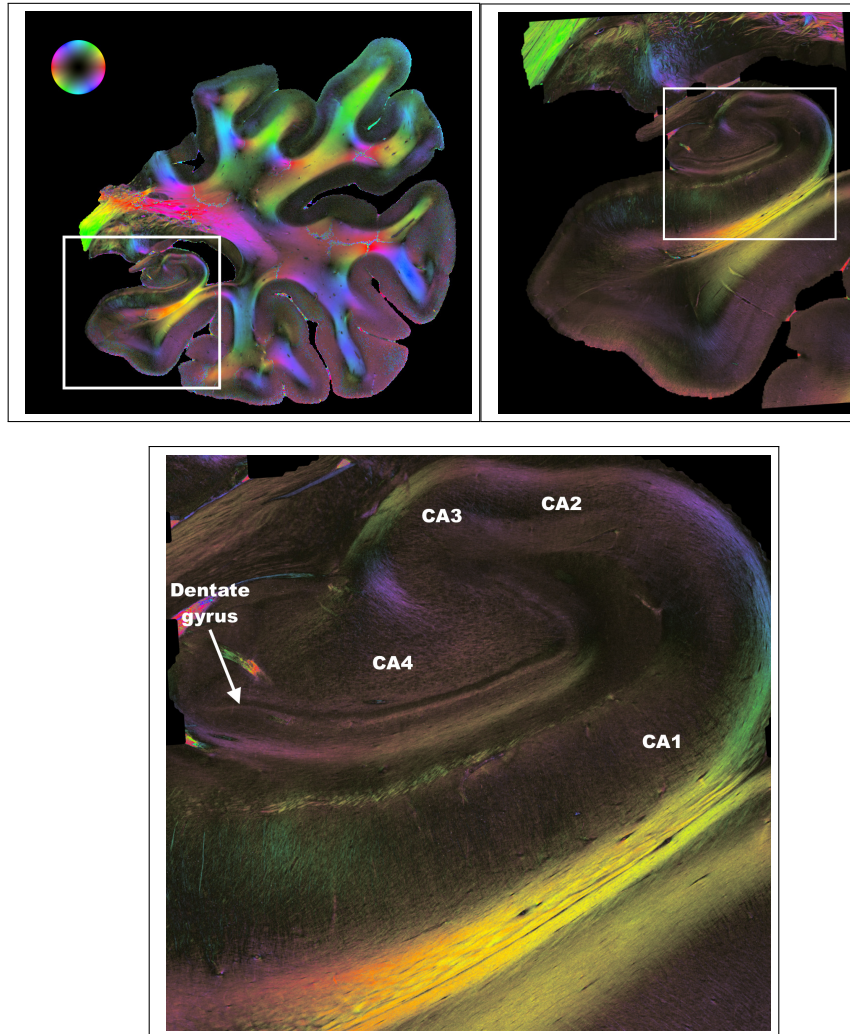


Figure 17: Fiber orientation maps (FOMs) obtained from registered high-resolution (top left) and ultra-high resolution (top right) 3D-PLI images (direction and inclination images) of Fig 1. The FOM of the enlarged region of the ultra-high resolution image (bottom) includes different human hippocampal subregions (CA1-4) at  $1.3 \mu m$  resolution.

sectioning and mounting process, it is important to use an elastic deformation model for tissues. Other methods using B-splines [13] or the demons [7] are not based on a physical deformation model, and are limited by the chosen grid or are not well suited for large deformations. In addition, the image similarity metric

for registration and the type of regularization need to be well adapted to the special characteristics of multi-modal 3D-PLI data. Unlike [6, 11], where macro-scale data (1 mm and 200  $\mu m$ , respectively) of the hippocampus was used, we consider *micro-scale* (1.3  $\mu m$ ) resolution 3D-PLI data. At this ultra-high resolution, an image covers a much smaller brain region compared to a corresponding high-resolution image (64  $\mu m$ ) (see Fig. 2). This increases the difficulty of the registration task (scaling factor of about 49). To cope with this problem we use a feature-based localization and registration approach. To our knowledge, it is the first time that uHR 3D-PLI images (1.3  $\mu m$ ) were used for 3D reconstruction, and that large stacks of HR and uHR images (0.88 cm in  $z$ -direction) were considered. Moreover, we proposed a physically-based elastic registration method in conjunction with a robust multi-modal similarity metric and a scale-adaptive technique to cope with both small and large deformations as well as a robust feature-based localization method for coherent 3D reconstruction.

In Section 3, we presented our non-rigid registration method (GEBS-CnCoT) which relies on a physical deformation model. The proposed method is based on Gaussian elastic body splines (which are solutions of the Navier equation from the theory of elasticity), it exploits the canonical correlation transform CnCoT for the image similarity metric, and comprises efficient regularizers. The advantage of the proposed CnCoT is that it integrates neighborhood information which increases the robustness of the data term (similarity measure). The main reason for improvement in accuracy and robustness (see Tab. 1, lowest mean TRE for 10 different 3D-PLI sections evaluated at different scales) is that the self-similarity of the patches is exploited in contrast to using information at single pixels (GEBS-CoT) [23]. Whereas in [42, 43] image gradient information is used for self-similarity, we here use the canonical correlation transform. This has the advantage that the intensity information is directly exploited, and, moreover, the computation of the patch matrices is fast and numerically stable. This is very important in our application of registering challenging multi-modal 3D-PLI image data. We demonstrated that our proposed method is well-suited for registration of the multi-modal 3D-PLI data and better handles complex

deformations compared to previous methods (e.g., [36, 37, 35, 23]). We found that GEBS-CnCoT well copes with both large and small deformations and yields  
570 accurate registration results. In Section 4, we proposed an extension of GEBS-CnCoT by a scale-adaptive method to handle large semi-global deformations due to tissue splits in some histological sections.

The uHR images ( $1.3 \mu m$ ) need to be first localized and then registered to the region-of-interest within the corresponding HR images or blockface images  
575 ( $64 \mu m$ ) as is evident from Fig. 2. To this end, we presented a feature-based approach for localization and registration of uHR images in Section 5. The approach was validated and compared with state-of-the-art feature extraction methods including SURF [39], SIFT [44], ORB [45], detH [46], and AKAZE [47] (see Supplementary material). It turned out that our approach outperformed  
580 previous methods in terms of both accuracy (lowest TRE) and robustness (e.g., invariance to contrast and rotation changes). For initial alignment of the HR data to blockface data, we proposed a multi-modal rigid registration method based on the correlation transform. We also presented the complete pipeline for 3D reconstruction of both HR and uHR 3D-PLI data. For registration of uHR  
585 3D-PLI images to the reference blockface images we make use of the computed deformation fields from non-rigid registration of the HR images to the blockface images (see Figs. 8 and 9). In addition, to cope with time delays of HR and uHR image acquisition, we perform non-rigid registration of the uHR images with the blockface images using GEBS-CnCoT (see Fig. 8).

590 Our proposed registration method was applied to 126 consecutive sections of the 3D-PLI data of the temporal lobe of the human brain. We performed a quantitative performance evaluation using 10 different 3D-PLI images (both HR and uHR data) and more than 1200 ground truth landmarks (about 106 landmarks per section for the HR data and about 23 landmarks per section for  
595 the uHR data). The results presented in Tab. 1 revealed that the proposed non-rigid registration method considerably improves the registration accuracy compared to existing non-rigid registration methods. The registration accuracy of GEBS-CnCoT is much better (3.3 pixels and 4.8 pixels for HR and uHR

data, respectively) compared to the state-of-the-art methods ANTS-CC [37]  
600 using  $z$ -normalized images (8.9 pixels and 11.5 pixels for HR and uHR data,  
respectively), and ANTS-SyN-MI [36, 37] using mutual information and dif-  
feomorphic transformations (6.3 pixels and 9.4 pixels for HR and uHR data,  
respectively). In addition, the proposed GEBS-CnCoT registration can cope  
with missing tissue parts and tissue ruptures as demonstrated in Fig. 11 (third  
605 row) while many existing non-rigid registration methods are misled by missing  
tissue as reported in [19].

In our registration method, prior rigid registration is performed for coarse  
alignment of the HR images (which tackles arbitrary rotations and translations  
of the sections, see Fig. 7 (c-e) and Fig. 12 (top)) and subsequently non-rigid  
610 GEBS-CnCoT registration is used to improve the result (see Fig. 7 (f-h) and  
Fig. 12 (bottom)). Visual assessment of the registered HR images showed a  
coherent alignment of sulci and gyri (Fig. 12, bottom left) which qualitatively  
validates the effectiveness of the proposed method. The quality of the registra-  
tion of HR 3D-PLI data was also confirmed by the coherent alignment of the  
615 white matter as can be seen in Fig. 14. Regarding the registration quality of the  
uHR images (hippocampus region), orthogonal views of the 3D reconstructed  
volume revealed that the registered uHR data agrees well with the reference  
blockface volume (Fig. 15). Corresponding brain structures are located at sim-  
ilar positions in both the uHR volume and the blockface volume indicated by  
620 the cross-hair labelled in blue (dentate gyrus at the top, and cornu ammonis at  
the bottom). The coherence of the brain structures can also be observed in the  
3D reconstructed uHR volume presented in Fig. 16.

In future work, we will extend our method to better cope with sections with  
missing tissue parts by exploiting information from other 3D-PLI modalities.  
625 Based on the reconstructed 3D volumes, fiber tracking could be performed to  
determine the human brain connectome. We also plan to identify and localize  
hippocampus regions in the reconstructed 3D volumes at multiple resolutions  
which are interesting for neuroscientists. Furthermore, we will use our registra-  
tion method for 3D reconstruction of 3D-PLI data of other primate brains such

630 as vervet and rat.

## 9. Conclusions

We have presented a novel non-rigid registration method as well as a complete pipeline for 3D reconstruction of both high-resolution ( $64 \mu m$ ) and ultra-high resolution ( $1.3 \mu m$ ) 3D-PLI data. We introduced a new similarity metric for spline-based non-rigid registration using the canonical correlation transform which is well-suited for multi-modal 3D-PLI registration. In addition, we introduced a normalized separable filter and structure preserving diffusion for regularization of the deformation fields. We also proposed a scale-adaptive non-rigid registration method to tackle large semi-global deformations due to tissue splits. A rigid registration approach based on a correlation transform metric was introduced for robust coarse alignment of high-resolution 3D-PLI images. We also described a feature-based localization and registration approach for ultra-high resolution 3D-PLI images. Advantages of the presented method compared to existing methods were demonstrated using both synthetic data and 3D-PLI data. Our quantitative and qualitative assessments revealed that the proposed registration method is well-suited for coherent 3D reconstruction of 3D-PLI data.

## Acknowledgments

This project was funded by the Helmholtz Association through the Helmholtz Portfolio theme “Supercomputing and Modeling for the Human Brain“ and by the European Union through the Horizon 2020 Research and Innovation Programme under Grant Agreement No. 7202070 (Human Brain Project SGA1). We gratefully acknowledge the computing time granted by the John von Neumann Institute for Computing (NIC) and provided on the supercomputer JU-RECA at the Jülich Supercomputing Centre (JSC). We would like to thank David Gräßel, Philipp Schlöme, and Martin Schober for data preparation, and Artjom Zern for his help during the revision of this manuscript.

## Supplementary material

Supplementary material related to this article can be found at [https://drive.google.com/open?id=1DcMQbnX3PI7x1kLpINuA5aJLfF\\_kcJn](https://drive.google.com/open?id=1DcMQbnX3PI7x1kLpINuA5aJLfF_kcJn)

## Appendix A.

The energy  $E(\mathbf{u}, \mathbf{u}^I)$  in Eq. (1) is minimized w.r.t.  $\mathbf{u}$  when  $\frac{\partial E}{\partial \mathbf{u}} = \mathbf{0}$ . Differentiating the quadratic regularization term in Eq. (8) w.r.t.  $\mathbf{u}$  yields

$$\lambda_I \frac{\partial(\psi_I)}{\partial \mathbf{u}} = 2\lambda_I \int f_{\sigma,\alpha}(\mathbf{x} - \xi)(\mathbf{u}^I(\xi) - \mathbf{u}(\mathbf{x}))d\xi \quad (\text{A.1})$$

Differentiating the elastic regularization term in Eq. (7) w.r.t.  $\mathbf{u}$ , we have

$$\lambda_E \frac{\partial(\psi_{elastic})}{\partial \mathbf{u}} = \lambda_E \mu \Delta \mathbf{u} + (\lambda + \mu) \nabla (\text{div } \mathbf{u}) \quad (\text{A.2})$$

Thus, we obtain

$$\frac{\partial E}{\partial \mathbf{u}} = \mu \Delta \mathbf{u} + (\lambda + \mu) \nabla (\text{div } \mathbf{u}) + \epsilon_I \int f_{\sigma,\alpha}(\mathbf{x} - \xi)(\mathbf{u}^I(\xi) - \mathbf{u}(\mathbf{x})) d\xi = \mathbf{0}, \quad (\text{A.3})$$

where  $\epsilon_I = 2 \frac{\lambda_I}{\lambda_E}$ .

## References

- [1] M. Axer, K. Amunts, D. Gräßel, C. Palm, J. Dammers, H. Axer, U. Pietrzyk, K. Zilles, A novel approach to the human connectome: Ultra-high resolution mapping of fiber tracts in the brain, *NeuroImage* 54 (2) (2011) 1091 – 1101. doi:10.1016/j.neuroimage.2010.08.075.
- [2] M. Axer, D. Gräßel, M. Kleiner, J. Dammers, T. Dickscheid, J. Reckfort, T. Hütz, B. Eiben, U. Pietrzyk, K. Zilles, K. Amunts, High-resolution fiber tract reconstruction in the human brain by means of three-dimensional polarized light imaging, *Frontiers in Neuroinformatics* 5 (34) (2011) 1–13. doi:10.3389/fninf.2011.00034.
- [3] J. Reckfort, H. Wiese, U. Pietrzyk, K. Zilles, K. Amunts, M. Axer, A multiscale approach for the reconstruction of the fiber architecture of the human brain based on 3D-PLI, *Frontiers in neuroanatomy* 9 (2015) 118.

- [4] T. Ragan, L. R. Kadiri, K. U. Venkataraju, K. Bahlmann, J. Sutin, J. Taranda, I. Arganda-Carreras, Y. Kim, H. S. Seung, P. Osten, Serial two-photon tomography: an automated method for ex-vivo mouse brain imaging, *Nat Methods* 9 (3) (2012) 255–258. doi:10.1038/nmeth.1854.
- 680 [5] J. Augustinack, K. Helmer, K. Huber, S. Kakunoori, L. Zöllei, B. Fischl, Direct visualization of the perforant pathway in the human brain with ex vivo diffusion tensor imaging, *Frontiers in Human Neuroscience* 4 (42) (2010) 1–13. doi:10.3389/fnhum.2010.00042.
- 685 [6] K. Amunts, O. Kedo, M. Kindler, P. Pieperhoff, H. Mohlberg, N. Shah, U. Habel, F. Schneider, K. Zilles, Cytoarchitectonic mapping of the human amygdala, hippocampal region and entorhinal cortex: intersubject variability and probability maps, *Anatomy and Embryology* 210 (5) (2005) 343–352. doi:10.1007/s00429-005-0025-5.
- [7] C. Palm, M. Axer, D. Gräbel, J. Dammers, J. Lindemeyer, K. Zilles, U. Pietrzyk, K. Amunts, Towards ultra-high resolution fibre tract mapping of the human brain - registration of polarised light images and reorientation of fibre vectors, *Frontiers in Human Neuroscience* 4 (9) (2010) 1–16. doi:10.3389/neuro.09.009.2010.
- 690 [8] J. Lebenberg, A.-S. Hérard, A. Dubois, J. Dauguet, V. Frouin, M. Dhenaina, P. Hantraye, T. Delzescaux, Validation of MRI-based 3D digital atlas registration with histological and autoradiographic volumes: An anatomofunctional transgenic mouse brain imaging study, *NeuroImage* 51 (2010) 1037–1046. doi:10.1016/j.neuroimage.2010.03.014.
- 695 [9] A. S. Choe, Y. Gao, X. Li, K. B. Compton, I. Stepniewska, A. W. Anderson, Accuracy of image registration between MRI and light microscopy in the ex vivo brain, *Magnetic Resonance Imaging* 29 (5) (2011) 683–692. doi:10.1016/j.mri.2011.02.022.
- 700 [10] K. Amunts, C. Lepage, L. Borgeat, H. Mohlberg, T. Dickscheid, M.-E. Rousseau, S. Bludau, P.-L. Bazin, L. Lewis, A.-M. Oros-Peusquens,

- 705 N. Shah, T. Lippert, K. Zilles, A. Evans, BigBrain: An Ultrahigh-Resolution 3D Human Brain Model, *Science* 340 (2013) 1472–1475. doi:10.1126/science.1235381.
- [11] D. H. Adler, J. Pluta, S. Kadivar, C. Craige, J. C. Gee, B. B. Avants, P. A. Yushkevich, Histology-derived volumetric annotation of the human  
710 hippocampal subfields in postmortem MRI, *NeuroImage* 84 (2014) 505 – 523. doi:10.1016/j.neuroimage.2013.08.067.
- [12] C.-W. Wang, E. Budiman Gosno, Y.-S. Li, Fully automatic and robust 3D registration of serial-section microscopic images, *Sci. Rep.* 5 (2015) 1–14. doi:10.1038/srep15051.
- 715 [13] N. Schubert, M. Axer, M. Schober, A. Huynh, M. Huysegoms, N. Palomero-Gallagher, J. G. Bjaalie, T. B. Leergaard, M. E. Kirlangic, K. Amunts, K. Zilles, 3D reconstructed cyto-, muscarinic m2 receptor, and fiber architecture of the rat brain registered to the waxholm space atlas, *Frontiers in Neuroanatomy* 10 (51) (2016) 1–13. doi:10.3389/fnana.2016.00051.
- 720 [14] P. Majka, D. Wójcik, Possum—A Framework for Three-Dimensional Reconstruction of Brain Images from Serial Sections, *Neuroinformatics* 14 (3) (2016) 265–278. doi:10.1007/s12021-015-9286-1.
- [15] J.-P. Thirion, Image matching as a diffusion process: an analogy with maxwell’s demons, *Medical Image Analysis* 2 (3) (1998) 243–260. doi:  
725 [http://dx.doi.org/10.1016/S1361-8415\(98\)80022-4](http://dx.doi.org/10.1016/S1361-8415(98)80022-4).
- [16] D. Rueckert, L. I. Sonoda, C. Hayes, D. L. G. Hill, M. O. Leach, D. J. Hawkes, Nonrigid registration using free-form deformations: application to breast mr images, *IEEE Transactions on Medical Imaging* 18 (8) (1999) 712–721. doi:10.1109/42.796284.
- 730 [17] S. Gefen, O. J. Tretiak, J. Nissanov, Elastic 3D alignment of rat brain histological images, *IEEE Trans. on Medical Imaging* 22 (11) (2003) 1480–9. doi:10.1109/TMI.2003.819280.

- [18] S. Ourselin, A. Roche, G. Subsol, X. Pennec, N. Ayache, Reconstructing a 3D structure from serial histological sections, *Image and Vision Computing* 19 (1) (2001) 25 – 31. doi:10.1016/S0262-8856(00)00052-4. 735
- [19] V. Arsigny, X. Pennec, N. Ayache, Polyrigid and polyaffine transformations: A new class of diffeomorphisms for locally rigid or affine registration, in: Proc. 6th Internat. Conf. on Medical Image Computing and Computer-Assisted Intervention (MICCAI), Montréal, Canada, November 15-18, 2003, pp. 829–837. doi:10.1007/978-3-540-39903-2\_101. 740
- [20] M. M. Zeineh, N. Palomero-Gallagher, M. Axer, D. Gräßel, M. Goubran, A. Wree, R. Woods, K. Amunts, K. Zilles, Direct visualization and mapping of the spatial course of fiber tracts at microscopic resolution in the human hippocampus, *Cerebral Cortex* 27 (3) (2017) 1779–1794. doi:10.1093/cercor/bhw010. 745
- [21] T. M. Shepherd, E. Ozarslan, A. T. Yachnis, M. A. King, S. J. Blackband, Diffusion tensor microscopy indicates the cytoarchitectural basis for diffusion anisotropy in the human hippocampus, *American J. of Neuroradiology* 28-5 (2007) 958–64.
- [22] B. Fischl, A. A. Stevens, N. Rajendran, B. T. Yeo, D. N. Greve, K. V. Leemput, J. R. Polimeni, S. Kakunoori, R. L. Buckner, J. Pacheco, D. H. Salat, J. Melcher, M. P. Frosch, B. T. Hyman, P. E. Grant, B. R. Rosen, A. J. van der Kouwe, G. C. Wiggins, L. L. Wald, J. C. Augustinack, Predicting the location of entorhinal cortex from MRI, *NeuroImage* 47 (1) (2009) 8 – 17. doi:10.1016/j.neuroimage.2009.04.033. 750 755
- [23] S. Ali, K. Rohr, M. Axer, D. Gräßel, P. Schlömer, K. Amunts, R. Eils, S. Wörz, Elastic registration of high-resolution 3D PLI data of the human brain, in: Proc. 14th IEEE Internat. Symposium on Biomedical Imaging (ISBI), Melbourne, Australia, April 18-21, 2017, pp. 1151–1155. doi:10.1109/ISBI.2017.7950720. 760

- [24] M. Schober, P. Schlömer, M. Cremer, H. Mohlberg, A.-M. Huynh, N. Schubert, M. Kirlangic, K. Amunts, M. Axer, Reference Volume Generation for Subsequent 3D Reconstruction of Histological Sections, in: Proc. Workshop Bildverarbeitung für die Medizin (BVM), Lübeck, Germany, Informatik aktuell, Springer Berlin Heidelberg, 2015, pp. 143–148. doi: 10.1007/978-3-662-46224-9\_26.
- [25] M. Schober, M. Axer, M. Huysegoms, N. Schubert, K. Amunts, T. Dickscheid, Morphing image masks for stacked histological sections using laplace’s equation, in: T. Tolxdorff, T. M. Deserno, H. Handels, H.-P. Meinzer (Eds.), Bildverarbeitung für die Medizin 2016: Algorithmen – Systeme – Anwendungen, Springer Berlin Heidelberg, 2016, pp. 146–151.
- [26] S. Wörz, K. Rohr, Spline-Based Hybrid Image Registration using Landmark and Intensity Information based on Matrix-Valued Non-Radial Basis Functions, *Internat. J. of Computer Vision* 106 (1) (2014) 76–92. doi:10.1007/s11263-013-0642-z.
- [27] J. Kohlrausch, K. Rohr, H. Stiehl, A New Class of Elastic Body Splines for Nonrigid Registration of Medical Images, *J. of Mathematical Imaging and Vision* 23 (3) (2005) 253–280. doi:10.1007/s10851-005-0483-7.
- [28] R. T. Whitaker, X. Xue, Variable-conductance, level-set curvature for image denoising, in: Proc. 2001 Internat. Conf. on Image Processing (ICIP), Vol. 3, 2001, pp. 142–145.
- [29] S. Ali, K. Rohr, D. Gräbel, P. Schlömer, K. Amunts, R. Eils, M. Axer, S. Wörz, Spline-based multimodal image registration of 3D PLI data of the human brain, in: Proc. Workshop Bildverarbeitung für die Medizin (BVM), Heidelberg, Germany, Informatik Aktuell, Springer Berlin Heidelberg, 2017, pp. 268–273. doi:10.1007/978-3-662-54345-0\_61.
- [30] M. Drulea, S. Nedevschi, Motion Estimation Using the Correlation Transform, *IEEE Trans. on Image Processing* 22 (8) (2013) 3260–3270. doi:10.1109/TIP.2013.2263149.

- 790 [31] P. Chou, N. Pagano, *Elasticity – Tensor, Dyadic, and Engineering Approaches*, Dover Publications, Inc., Mineola, NY/USA, 1992.
- [32] P. Cachier, N. Ayache, Isotropic Energies, Filters and Splines for Vector Field Regularization, *J. of Mathematical Imaging and Vision* 20 (3) (2004) 251–265. doi:10.1023/B:JMIV.0000024042.88755.4f.
- 795 [33] D. Marquardt, An Algorithm for Least-Squares Estimation of Nonlinear Parameters, *J. of the Society for Industrial and Applied Mathematics* 11 (2) (1963) 431–441. doi:10.1137/0111030.
- [34] W. Press, B. Flannery, S. Teukolsky, W. Vetterling, *Numerical Recipes in C*, Cambridge University Press, Cambridge, UK, 1992.
- 800 [35] A. Biesdorf, S. Wörz, H.-J. Kaiser, C. Stippich, K. Rohr, Hybrid Spline-Based Multimodal Registration using Local Measures for Joint Entropy and Mutual Information, in: *Proc. 12th Internat. Conf. on Medical Image Computing and Computer-Assisted Intervention (MICCAI)*, Vol. 5761 of *Lecture Notes in Computer Science*, Springer Berlin Heidelberg, London, UK, 2009, pp. 607–615.
- 805 [36] B. Avants, C. Epstein, M. Grossman, J. Gee, Symmetric diffeomorphic image registration with cross-correlation: Evaluating automated labeling of elderly and neurodegenerative brain, *Medical Image Analysis* 12 (1) (2008) 26 – 41. doi:https://doi.org/10.1016/j.media.2007.06.004.
- 810 [37] B. B. Avants, N. J. Tustison, G. Song, P. A. Cook, A. Klein, J. C. Gee, A reproducible evaluation of ANTs similarity metric performance in brain image registration, *NeuroImage* 54 (3) (2011) 2033–2044. doi:10.1016/j.neuroimage.2010.09.025.
- 815 [38] S. Ali, K. Rohr, M. Axer, K. Amunts, R. Eils, S. Wörz, Registration of ultra-high resolution 3D PLI data of human brain sections to their corresponding high-resolution counterpart, in: *Proc. 14th IEEE Internat. Sym-*

posium on Biomedical Imaging (ISBI), Melbourne, Australia, April 18-21, 2017, pp. 415–419. doi:10.1109/ISBI.2017.7950550.

- [39] H. Bay, A. Ess, T. Tuytelaars, L. Van Gool, Speeded-up robust features (SURF), *Computer Vision and Image Understanding* 110 (2008) 346–359. doi:10.1016/j.cviu.2007.09.014.
- [40] M. Muja, D. G. Lowe, Scalable Nearest Neighbor Algorithms for High Dimensional Data, *IEEE Trans. on Pattern Analysis and Machine Intelligence* 36 (11) (2014) 2227–2240. doi:10.1109/TPAMI.2014.2321376.
- [41] P. Thévenaz, U. Ruttimann, M. Unser, A Pyramid Approach to Subpixel Registration based on Intensity, *IEEE Trans. on Image Processing* 7 (1) (1998) 27–41. doi:10.1109/83.650848.
- [42] S. Ali, C. Daul, E. Galbrun, W. Blondel, Illumination invariant optical flow using neighborhood descriptors, *Computer Vision and Image Understanding* 145 (2016) 95–110. doi:10.1016/j.cviu.2015.12.003.
- [43] L. Bao, Q. Yang, H. Jin, Fast edge-preserving patchmatch for large displacement optical flow, *IEEE Trans. on Image Processing* 23 (12) (2014) 4996–5006. doi:10.1109/TIP.2014.2359374.
- [44] D. Lowe, Distinctive Image Features from Scale-Invariant Keypoints, *Internat. J. of Computer Vision* 60 (2) (2004) 91–110. doi:10.1023/B:VISI.0000029664.99615.94.
- [45] E. Rublee, V. Rabaud, K. Konolige, G. Bradski, ORB: An efficient alternative to SIFT or SURF, in: *Proc. of Internat. Conf. on Computer Vision (ICCV)*, IEEE Computer Society, Washington D.C., USA, 2011, pp. 2564–2571. doi:10.1109/ICCV.2011.6126544.
- [46] T. Lindeberg, Image matching using generalized scale-space interest points, *J. of Mathematical Imaging and Vision* 52 (1) (2015) 3–36. doi:10.1007/s10851-014-0541-0.

- [47] P. F. Alcantarilla, J. Nuevo, A. Bartoli, Fast explicit diffusion for accelerated features in nonlinear scale spaces, in: Proc. of British Machine Vision Conf. (BMVC), Bristol, UK, 2013, pp. 13.1–13.11.